Zitierweise: Angew. Chem. Int. Ed. **2021**, *60*, 122–141
Internationale Ausgabe: doi.org/10.1002/anie.202009449
Deutsche Ausgabe: doi.org/10.1002/ange.202009449

Nanohybrids

Fullerenes as Key Components for Low-Dimensional (Photo)electrocatalytic Nanohybrid Materials

Alain R. Puente Santiago[+],* *Olivia Fernandez-Delgado*[+], *Ashley Gomez*,
*Md Ariful Ahsan and Luis Echegoyen**

Stichwörter:
(photo)electrocatalysis · fullerene ·
HER · nanohybrids · OER

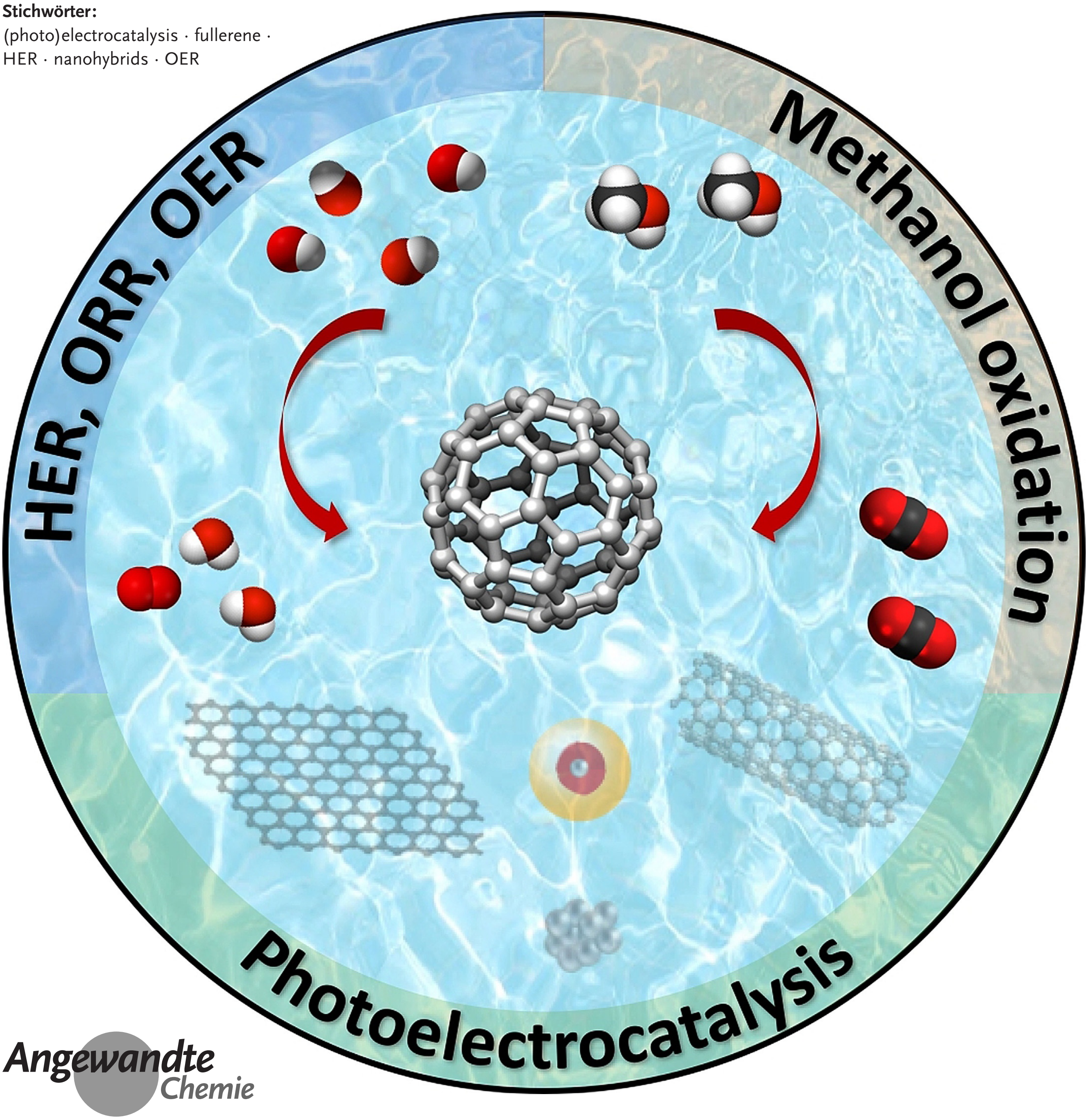

An emerging class of heterostructures with unprecedented (photo)-electrocatalytic behavior, involving the combination of fullerenes and low-dimensional (LD) nanohybrids, is currently expanding the field of energy materials. The unique physical and chemical properties of fullerenes have offered new opportunities to tailor both the electronic structures and the catalytic activities of the nanohybrid structures. Here, we comprehensively review the synthetic approaches to prepare fullerene-based hybrids with LD (0D, 1D, and 2D) materials in addition to their resulting structural and catalytic properties. Recent advances in the design of fullerene-based LD nanomaterials for (photo)electrocatalytic applications are emphasized. The fundamental relationship between the electronic structures and the catalytic functions of the heterostructures, including the role of the fullerenes, is addressed to provide an in-depth understanding of these emerging materials at the molecular level.

Aus dem Inhalt

1. Introduction

Low-dimensional materials have attracted considerable attention for (photo)electrocatalytic applications.[1–9] Unlike their bulk-counterparts, they exhibit more favorable electronic properties with enhanced catalytic activities, owing to the effects of quantum confinement on the electronic density of states. The quantum confinement at the nanometric level can enable the downshift of the center of the d-band relative to the energy of the Fermi level, which, in turn, decreases the adsorption energy of the intermediate catalytic reactants, thus improving the catalytic efficiency.[11–18] Quantum confinement contributes to the increase in the photocatalytic activity by favoring photon absorption processes and shifting the valence and conduction bands. However, despite the singular electronic properties of low-dimensional (LD) materials, they are predominantly anisotropic, which fairly limits their practical applications. Many approaches have been attempted to hybridize them with other nanostructured materials via covalent and non-covalent strategies.[19–23] The assembly of LD nanomaterial units has given rise to different types of heterostructures with enhanced catalytic properties, such as 0D–1D, 0D–2D, 1D–2D, and 2D–2D.[25] The resulting nanohybrids have shown unique (opto)electronic properties, a large number of low-coordination sites, and huge surface area-to-volume ratios, which notably improve the activity, selectivity, and Faradaic efficiencies of a large number of electro- and photocatalytic reactions.[26–35]

Among the large portfolio of LD structures, fullerenes have played a crucial role in the development of highly efficient catalysts.[36,37] Since the discovery of buckyballs by Kroto et al. in 1985,[38] the first known 0D nanocarbon compound, a large number of fullerene-based nanoheterostructures have been developed based on the unique electron-accepting properties of fullerenes, as well as their ability to act as effective building blocks to form functional supramolecular assemblies.[39–42] The hybridization of fullerenes with LD nanomaterials, such as quantum dots, nanoparticles, graphene, and graphitic carbon nitride (g-C_3N_4) nanosheets, to fabricate highly active (photo)electrocatalytic systems has notably sparked the interest of both the materials science and the catalysis communities. Fullerene-based LD hybrids have emerged as highly efficient metal-free energy conversion systems as well as potentially inexpensive alternatives to replace Pt and compete with state-of-the-art (photo)electrocatalysts, offering a combination of low cost, high activity, and superior stability.[43–46] The catalytic properties of the resulting nanohybrids are governed by their electronic structures. The Sabatier principle states that the interactions of the reactant and intermediate species with the catalytically active surfaces should be driven by moderate energy adsorption values instead of strong or weak interfacial interactions. According to this rule, the electronic behavior at the molecular level and, thus, the catalytic activity of the resulting fullerene-based LD heterostructures can be effectively tuned by engineering the morphology, composition, defect density, and strain. Accordingly, the electrocatalytic and (photo)electrocatalytic performances of fullerene-based LD materials can be modulated by changing the density of fullerenes in the nanostructured framework, the dimensionality of the nanomaterial tied to the fullerene, and/or the number of defects on the resulting composites. For instance, the rational design of 0D–2D heterostructures composed of C_{60} adsorbed onto single-walled carbon nanotubes through van der Waals (vdW) interactions has been elegantly used to fabricate metal-free

---

[*] Dr. A. R. Puente Santiago,[+] O. Fernandez-Delgado,[+] A. Gomez,
M. A. Ahsan, Prof. L. Echegoyen
Department of Chemistry and Biochemistry
University of Texas at El Paso
500 West University Avenue, El Paso, Texas 79968 (USA)
E-Mail: arpuentesan@utep.edu
echegoyen@utep.edu

[+] These authors contributed equally to this work.

Supporting information (discussion of hybrids of C_{60} with other 2D materials) and the ORCID identification number(s) for the author(s) of this article can be found under:
https://doi.org/10.1002/anie.202009449.

multifunctional electrocatalysts.[47] The excellent electron affinity of C_{60} that enables the acquisition of up to 6 electrons per molecule has been used to induce intramolecular electron transfer processes from the single-walled carbon nanotubes (SWCNTs) to the adsorbed fullerenes to create high-performance catalytic active sites at the C_{60}/SWCNTs interfaces. Furthermore, the number of active sites and corresponding electrocatalytic activity has been strongly correlated to the number of adsorbed fullerenes. Among other examples are C_{60}/g-C_3N_4 0D–2D nanohybrids, which have shown remarkable photocatalytic activities by downshifting the relatively large band gap of 2.7 eV of the graphitic carbon nitride nanosheets as well as the electron–hole recombination rates, which strongly influence the overall kinetic efficiency.[48,49]

Shenfang and co-workers have summarized the structural properties and potential applications of the nanohybrids of fullerenes and 2D materials.[36] However, the aforementioned review article is mainly focused on 0D–2D fullerene-based nanohybrids for energy conversion/photocatalytic systems.

Consequently, a comprehensive analysis of the properties, synthetic methodologies, structures, and (photo)electrocatalytic performances of fullerene-based LD nanoheterostructures is needed.

In this Review we address the recent breakthroughs in the use of fullerenes as essential components of high-performance (photo)electrocatalytic low-dimensional nanohybrids. The synthetic strategies to fabricate fullerene–0D, fullerene–1D, and fullerene–2D hybrids, including their structural properties and (photo)electrocatalytic performances for water splitting and methanol oxidation reactions, are comprehensibly presented (Figure 1).

2. Fullerene–0D Nanomaterial Hybrids

2.1. Synthesis and Electronic Properties

2.1.1. C_{60}–QDs Heterostructures

Recent advances in the area of quantum dots (QDs) have shown their wide range of applications that extend from sensing[50] and bioimaging to catalytic water splitting owing to their remarkable electronic, electrochemical, optical, and catalytic properties.[51,52] The synthesis of QDs can be

Alain R. Puente Santiago received his PhD degree in Physical Chemistry with distinction from the University of Cordova, Spain in 2017. He is currently a postdoctoral fellow in Prof. Luis Echegoyen's group in the Chemistry Department of the University of Texas at El Paso. His research interests focus on the development of low-dimensional nanohybrids for electrocatalysis.

Md Ariful Ahsan received his M.Sc. from the Department of Chemistry, Tuskegee University, in 2015, under the supervision of Prof. Michael L. Curry. Currently, he is doing his Ph.D. at The University of Texas at El Paso, working with Prof. Juan C. Noveron. His research focuses on multifunctional nanomaterials for wastewater treatment and energy conversion technologies.

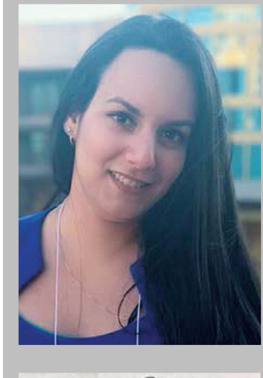

Olivia Fernandez-Delgado was born in Cuba (Havana) in 1993. She obtained her B.S. in Chemistry from the University of Havana in 2016. She is currently pursuing her Ph.D. in the group of Prof. Luis Echegoyen in the University of Texas at El Paso. Her research interests include the synthesis and characterization of new fullerene and carbon nano-onion derivatives for photovoltaic, catalytic, and biological applications.

Luis Echegoyen obtained both his BSc and PhD from the University of Puerto Rico in Rio Piedras. After several professorships at the Universities of Puerto Rico, Maryland, and Miami he was appointed Chair of the Department of Chemistry at Clemson University, in South Carolina. Later he served as Division Director for Chemistry at the National Science Foundation for 4 years (2006–2010) and more recently, he became the Robert A. Welch Professor of Chemistry at the University of Texas-El Paso in 2010. In 2018 he was elected President of the American Chemical Society. His research interests include fullerene chemistry, electrochemistry, and supramolecular chemistry.

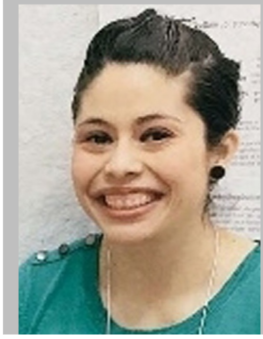

Ashley Gomez obtained a B.S. in Chemistry in 2018 from the University of Texas at El Paso. She is currently pursuing her M.A. degree as a shared student between Prof. Luis Echegoyen and Prof. Sreeprasad Sreenivasan's research groups. Her research interests include synthesis and characterization of mixed-metal cluster metallofullerenes to determine their single-molecule magnetic behavior, in addition to synthesizing 2D materials for perovskite solar cell applications.

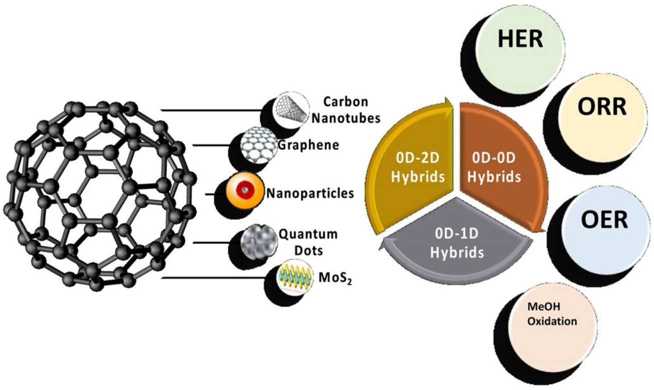

Figure 1. Summary of C_{60} nanohybrids described in this Review and their applications in catalysis.

achieved by two general methods: top-down or bottom-up approaches. With the top-down approach, a semiconductor is thinned until the QDs are formed. Wet chemical etching is generally used to obtain diameters of approximately 30 nm. One of the limitations of this method is the introduction of imperfections and impurities to the samples. An alternative methodology commonly used is reactive ion etching (RIE). In this method, reactive gas species are incorporated into an etching chamber and a radio frequency voltage is applied to produce a plasma that strikes the surface, forming a volatile product that etches a patterned sample. In the case of the bottom-up approach, there are four main techniques: microemulsion,[53–55] sol–gel,[56–59] hydrothermal methods[60–62] and hot-solution decomposition processes.[63–66] All of these constitute wet methods that mainly follow classical precipitation procedures by controlling several parameters, such as the concentration and temperature of the precursor solutions. Several reports have utilized vapor-phase methods to prepare QDs. The process begins by growing layers atom-by-atom, thus the QD growth can occur without patterning. The growth takes place in different ways: epitaxial growth,[67] formation of a smooth layer followed by nucleation and growth of small islands,[68] or the growth of small islands directly onto the substrate.[51]

One important aspect that can be tuned during QD synthesis is the introduction of small quantities of other materials. It has been shown that doping can alter the band structure by creating local quantum states that affect their (opto)electronic properties. Many transition metals have been introduced in QDs, such as Mn,[69] Cr,[70] Cu,[71] and Co.[72] A major drawback regarding their fabrication is the difficulty of controlling their size and distribution. A common solution is the utilization of capping-agents-like organic ligands, such as oleic acid or oleylamine.[73] Among the different materials used to dope QDs, carbon-based materials have attracted the most attention. It has been shown that the electron transfer mechanisms of the QDs/carbon-based hybrid materials vary significantly. The utilization of fullerenes has gained increasing attention because of their stability and overall physicochemical properties.[74–79] An interesting article was published in 2017 by Du et al. in which the authors synthesized C_{60} nanorods decorated with CdSe/CdS/ZnS QDs by liquid–liquid interfacial precipitation and studied the electronic properties of the hybrids.[80] The results of transmission electron microscopy coupled with Kelvin probe force microscopy (TEM/KPFM) revealed that the nanorods exhibit a roughly uniform morphology with dimensions of approximately 3–40 nm in length and 160–500 nm in diameter with no quantum dot aggregates. Based on the UV/Vis spectra, the intrinsic electronic transitions occur at 325 nm. Absorption peaks were also identified at 445 and 500 nm, which could be attributed to the 0D–0D hybrid's Frenkel and charge-transfer excitons. It must be noted that absorptions at wavelengths longer than 500 nm can be considered Frenkel excitons that include a strong phonon coupling. An emission decay profile was also conducted and it was consistent with the quenching observed by photoluminescence. The average emission lifetimes for the QDs and C_{60} nanorods were $<\tau> = 30.79$ and $<\tau> = 18.41$ ns, respectively, with an electron transfer efficiency of 40.21 %. The ultraviolet photoelectron spectroscopy (UPS) measurements showed the 0D–0D hybrid's valence band maximum at 6.2 and 5.8 eV, both below the vacuum level, while the conduction band minimum was estimated at 3.7 and 4.0 eV, also below vacuum. To facilitate the charge transport, octadecylamine was used as the ligand through which the electrons can tunnel via the QD conduction band to the conduction band of C_{60}. Most ligands exhibit insulating behavior, thus acting as a barrier for charge transport. As a result, this behavior causes charge accumulation as seen by spark plasma sintering (SPS). Three main regions were observed: at 320–420 nm (because of intramolecular transitions), at 420–550 nm (Frenkel/charge transfer excitons), and at 550–720 nm (strong coupling between excitons and phonons).

A C_{60}/QD hybrid with a different morphology was prepared by Yi and co-workers by synthesizing ZnO core–C_{60} shell QDs by a hydrothermal method using zinc acetate dihydrate in a dimethylformamide solution. ZnO@C_{60} QDs were prepared by the addition of C_{60} oxide to the same solution to obtain a size distribution of 10–20 nm (Figure 2 A).[10] The electronic structure was analyzed via UPS and the hybrid's measured secondary electron cutoff (SEC) region was at 3.73 eV. A higher work function was observed for the 0D–0D hybrid in comparison to the SEC region of pristine ZnO QDs at 3.48 eV. Owing to the significant difference in ZnO and C_{60} work functions, the electrons were transferred to C_{60}. As a result, as more ZnO was deposited, a gradual change in C_{60}'s SEC and highest occupied molecular orbital (HOMO) levels was observed. To confirm a possible energy shift, X-ray photoelectron spectroscopy (XPS) measurements showed a clear shift to higher binding energies. No further shift was detected in the flat band. ZnO QDs exhibited a higher charge density than C_{60} and a low ZnO–C_{60} volume ratio. Changes in ionization energy as electrons were transferred caused a further downward shift of the lowest unoccupied molecular orbital (LUMO) level of C_{60} just slightly above the Fermi level at 0.10 eV.

In addition to physical attachment and adsorption methods to prepare C_{60}/QD hybrids, Kamat et al. introduced the preparation of CdSe QDs chemically attached to thiol-functionalized C_{60} molecules to make a 0D–0D composite

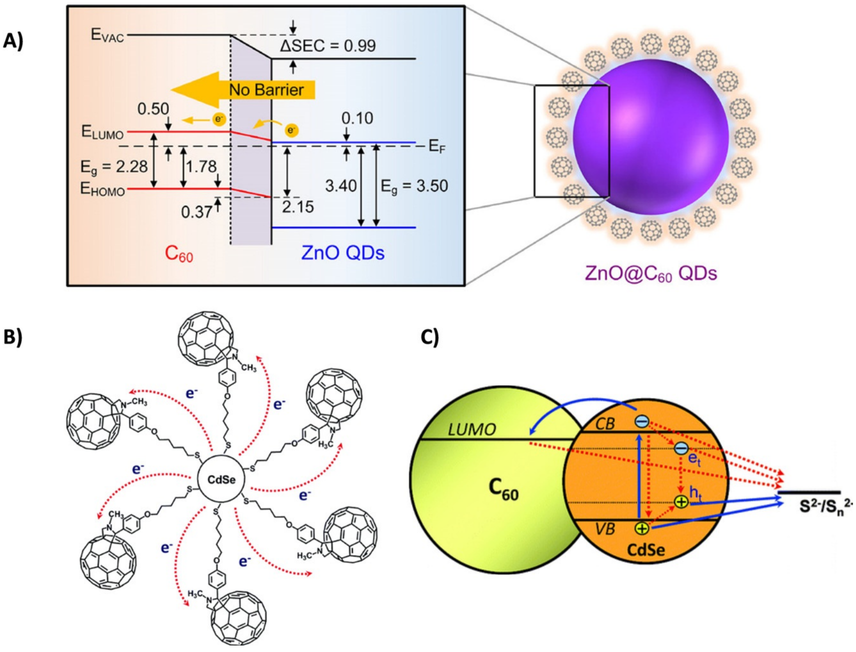

Figure 2. A) Schematic illustration of the electronic structure of ZnO core–C_{60} shell (ZnO@C_{60}) QDs.[10] Copyright 2017, American Chemical Society. B) Scheme of CdSe QD–C_{60} nanocomposite. C) Charge transfer processes in CdSe QD–C_{60} nanocomposites. Solid blue lines represent charge transfer processes required for photocurrent generation, whereas dotted, red lines depict main recombination paths that deteriorate the cell performance.[24] Copyright 2011, American Chemical Society.

(Figure 2B).[24] The electron transfer processes of this 0D–0D hybrid were further studied and it was found that the electrons are transferred from the CdSe QDs to the fullerenes (Figure 2B,C). Scanning electron microscopy (SEM) images display clusters of the 0D–0D material approximately 50–100 nm in diameter. It must be noted that the recovery time and overall charge transfer kinetics are directly dependent on the size of the QDs. For the smaller-sized QDs, the corresponding conduction band is less negative than that for the larger-sized QDs. In principle, the smaller the CdSe QDs, the faster the electron transfer upon coupling with C_{60}. The radical anion of C_{60} exhibits a decay time of approximately 50% more at 1.6 ns, which is consistent with the size-dependent incident photon-to-electron conversion efficiency (IPCE) measurements. For the larger QDs, the maximum IPCE was found to be 8%, while for the medium–small CdSe QDs it was 4%, thus the larger the QD, the higher the photocurrent generated.

2.1.2. *C_{60}–NPs Heterostructures*

Nanoparticles (NPs) are considered one of the most versatile 0D materials. Their applicability ranges from analytical chemistry, medicine, and environmental science to agriculture and the pharmaceutical industry. Some of their properties, such as surface area, size, and shape, strongly depend on the synthetic strategies. NPs can be synthesized similarly to QDs: by top-down or bottom-up approaches. In the top-down approach, the bulk material is broken down into smaller units that retain their overall composition.[81,82] Several techniques have been used in this approach, such as ball milling,[83,84] laser ablation,[85–89] ion sputtering,[90–92] and inert gas condensation.[93–95] The main drawback of this approach is the number of imperfections on the surface of the material. The bottom-up approaches consist of bringing building blocks together to form the NPs. Common methods used in this approach are chemical and electrochemical reductions, microwave-assisted synthesis,[96] co-precipitation,[97,98] sol–gel fabrication,[99] vapor-phase chemical deposition,[100] and hydrothermal synthesis.[101,102] However, multiple approaches have been used to improve the nanoparticles' properties. One common strategy is to form 0D–0D hybrids with fullerenes to enhance the conductivity and (opto)electronic properties of the NPs. One way to synthesize these 0D–0D hybrids is to covalently link a fullerene derivative to an as-synthesized nanoparticle. An article published in 2002 reported the synthesis of fullerene-functionalized gold nanoparticles (Au-S-C_{60}) used as photoactive antennas.[103] The C_{60} was functionalized with a thiol group by a 1,3-dipolar cycloaddition reaction. The gold NPs were prepared using a reported method but including 5 mg of the fullerene derivative with 21 mg of dodecanethiol. After precipitation of the Au-S-C_{60} NPs, the product was washed with ethanol and dried. TEM images showed Au-S-C_{60} clusters of various sizes ranging from 5 to 30 nm, indicating that the 0D–0D hybrid can also aggregate in nonpolar solvents. Atomic force microscopy (AFM) revealed that the morphology of the films displays a high surface area of 3D clusters. To measure the photoactivity, the 0D–0D hybrid film was used as the photoanode and applied on a SnO_2 electrode within a photoelectrochemical cell illuminated with visible light. The hybrid's ability to generate a photocurrent was confirmed by IPCE. To determine the reproducibility of the electrode, additional on–off cycles exhibited a photovoltage of 150 mV and a generated photocurrent of 130 $\mu A\,cm^{-2}$, thus confirming the ability of C_{60} to act as a photon absorber within the 0D–0D heterostructure.

Another interesting approach to synthesize fullerene–NP hybrids was reported by Basiuk et al. in 2008.[104] In this work, the authors first deposited C_{60} onto a Si wafer by physical vapor deposition. Then the layers of C_{60} were crosslinked with 1,8-diaminooctane gas, using 1 torr, at a temperature of 150 °C for 2 hours. The next step was the addition of the Ag NPs, prepared by the reduction of $AgNO_3$ with citric acid. Two solutions of $AgNO_3$ and citric acid in 2-propanol were added simultaneously to the reaction containing the C_{60} samples in 10 mL of 2-propanol. The reaction was stirred vigorously for 30 min at room temperature. The samples were then washed with 2-propanol to eliminate any excess reactants, then dried and stored under vacuum. SEM images showed clear differences for C_{60}-Ag/Si compared with the starting material because of the aggregation of Ag particles, causing a heterogeneous distribution of Ag clusters over the surface. For the C_{60}-DA-Ag/Si hybrid, the Ag clusters were homogeneously distributed because of the additional functionalization with the nitrogen atoms that act as nucleation sites for the clusters. The 1,8-diaminooctane moieties crosslinked the film's surfaces, thus reducing agglomeration and improving its homogeneity. Using reflectance spectroscopy, the band gaps for C_{60}-Ag/Si and C_{60}-DA-Ag/Si were consistent with the previously reported mobility gap (2.3 ± 0.1 eV). However, the C_{60}-DA/Si hybrid decreased the experimental error by 0.1 eV. Only the C_{60}-DA/Si hybrid displayed high photoluminescence. The Ag particles in the C_{60}-Ag/Si hybrid caused a significant decrease in quenching and only a slight increase in the C_{60}-DA-Ag/Si heterostructures. Internal quantum efficiency curves showed that the maximum wavelength obtained for (Au)C_{60}-Ag/Si was 850–900 nm. 0D–0D hybrid films (Au)C_{60}-DA/Si and (Au)C_{60}-DA-Ag/Si absorbed near 450 nm, exhibiting a significant decrease in the generated photocurrents, attributed to the charge recombination that occurs within the hybrids functionalized with 1,8-diaminooctane. Dark current–voltage characterization was also conducted, revealing no significant differences within the barriers of all three 0D–0D hybrids. However, there is a substantial increase in resistance for (Au)C_{60}-DA/Si and (Au)C_{60}-DA-Ag/Si when compared with (Au)C_{60}-Ag/Si. The influence of Ag particles produced a decrease in the transmittance of light, but importantly, there was no impact on the hybrid's photoelectric properties.

2.2. Catalytic Properties

Zero-dimensional nanostructured materials, such as nanoparticles and quantum dots, continue to attract interest because of their suitable properties for different types of catalytic reactions, such as their small sizes, large surface areas, and excellent charge transfer rates.[1,105–108] The assembly of fullerenes and 0D nanomaterials to build 0D–0D hybrids with efficient water-splitting catalytic properties has remained mostly unexplored. However, a few articles have shown potential applications of these nanohybrids for electrocatalysis. As one of the first approaches, Roth and co-workers synthesized fullerene–Pt nanoparticle assemblies (Figure 3 A–C) for methanol electrooxidation reactions.[109] The synergistic interactions between C_{60} and the Pt NPs facilitated the formation of active sites for the electrooxidation of small molecules like methanol. The fullerenes provided the ability to immobilize nanoparticles on the electrode surfaces and study their electrocatalytic performance.

The electronic properties of fullerene–0D nanomaterial heterostructures have been studied by connecting C_{60} molecules to gold surfaces via covalent chemistry.[110] For instance, a set of four thionoester- and thioketone-substituted azahomo-[60]fullerenes (Figure 4 A–C) was anchored on gold nanoparticle surfaces through Au–S covalent bonds, which exhibited impressive electron transfer properties. The C_{60}-functionalized AuNPs were highly efficient „electron sponge systems“ accepting up to an average of 4500 electrons via a lithium naphthalide-mediated process (Figure 3 D).[111] Although these nanohybrids were not tested as electrocatalysts, their improved electron mobility could be used to create electrocatalytic systems with superior electrochemical performances.

Fullerenes have been assembled in different ways to effectively accommodate nanoparticles to yield more energetically favorable active sites, which consequently increase their catalytic activity.[112,113] For instance, Pt nanoparticles were electrodeposited onto a two-dimensional array of fulleropyrrolidine (PyC_{60}, Figure 4 D) molecules to form high-performance electrocatalysts for the methanol oxidation reaction (MOR).[114] The Pt nanoparticles adopted a nanoflake-like structure at higher concentrations that was optimized by coulometric techniques. To evaluate the electrocatalytic activity of the Pt/PyC_{60} heterostructures, cyclic voltammetry (CV) was performed in 0.5 M H_2SO_4 and 0.5 M H_2SO_4 + 1.0 M MeOH solutions, respectively (Figure 3 E,F). Additionally, the Pt nanoflakes and Pt/C were tested under the same experimental conditions. The electrochemical surface area (ECSA) derived from the hydrogen adsorption–desorption charge processes was much larger for the Pt/PyC_{60} nanohybrid catalysts (Figure 3 E), indicating the presence of a larger number of catalytic active sites. In addition, Pt/PyC_{60} heterostructures delivered remarkable MOR activities, outperforming both the mass activity and specific activity values of both the unsupported Pt NPs and the commercial Pt/C (Figure 3 G). The Pt/PyC_{60} hybrids showed better electrochemical long-term stability than unsupported Pt NPs and commercial Pt (Figure 3 H). The improved catalytic performance was associated with the capacity of the fulleropyrrolidine nanosheets to uniformly distribute the Pt nanoflakes, thus increasing their electrochemically active surface areas, and, in turn, the number of active sites and the overall MOR activity. As another example of supramolecular fullerene structures for catalytic applications, highly ordered mesoporous fullerene nanostructures (MFC_{60}) were developed as excellent catalysts for the oxygen reduction reaction (ORR) using mesopore channels of SBA-15 silica as templates. The highly porous fullerene nanostructures considerably increased the number of ORR active sites through the addition of in-plane pores or nanopores within the carbon networks.[115,116] Recently, Vinu et al. have incorporated different amounts of Cu nanoparticles (5, 10, 20, and 25 %) into the mesoporous fullerene framework to construct new high-performance ORR catalysts.[44] The synergistic interaction between the MFC_{60} structure and the Cu NPs resulted in enhanced electrocatalytic yields. Figure 3 I,J shows the morphologies of the MFC_{60}–Cu NPs nanocomposites. MFC_{60} shows a non-homogeneous distribution of bundled rod-like structures with different sizes between 6 and 15 μm while the Cu nanoparticles are well-dispersed inside the porous fullerene framework. The nanoparticles exhibited a mixture of metallic and ionic Cu phases. The HRTEM and selected area electron diffraction (SAED) pattern confirmed a highly organized hexagonal fullerene crystalline lattice with well-defined fringes of 0.246 nm, which originated from the SBA-15 template (Figure 3 K,L). The Cu(15 %)–MFC_{60} catalyst

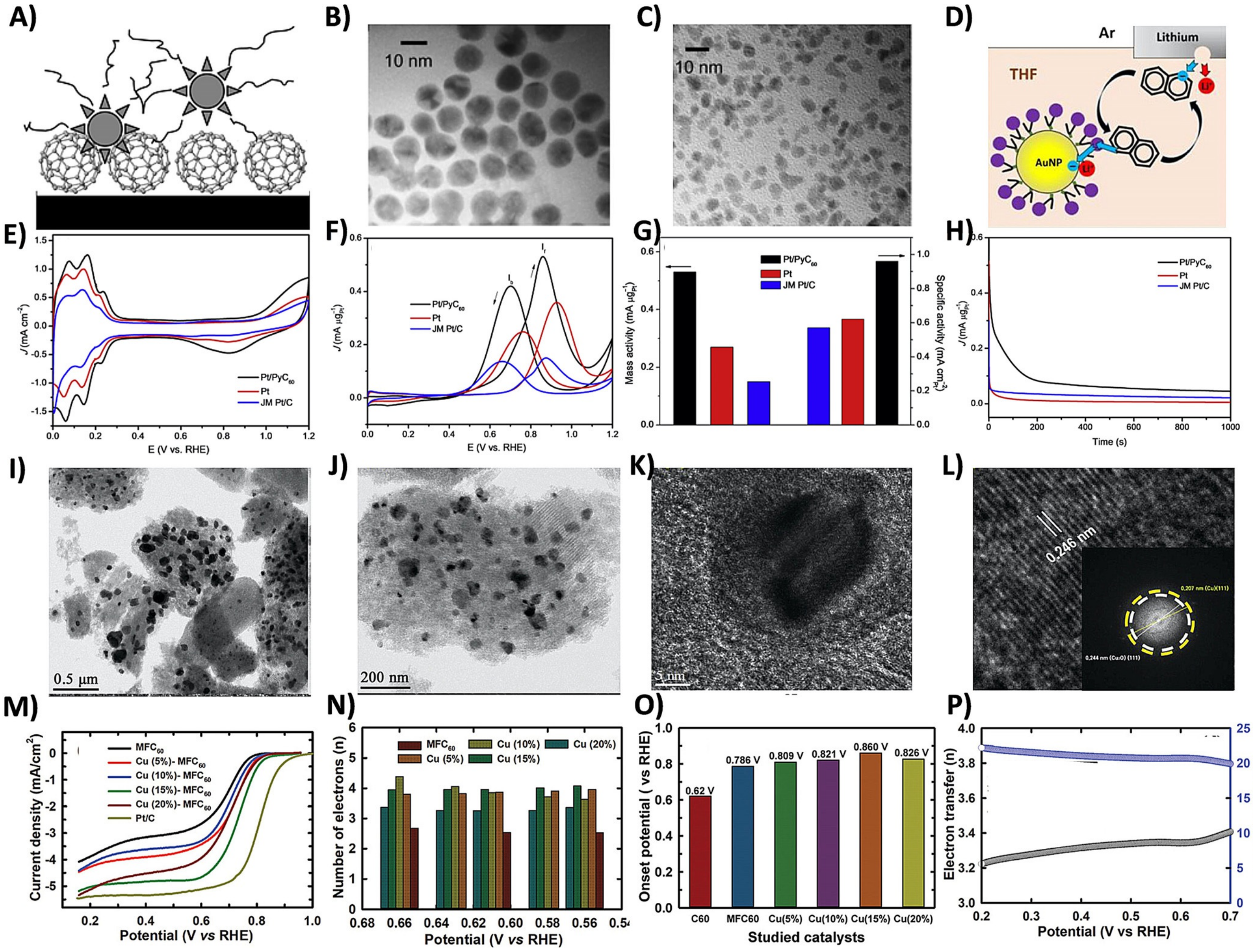

Figure 3. A) Schematic representation of fullerene-linked Pt nanoparticles. B) TEM pictures of TOAB–Pt in toluene. C) TEM pictures of PVP–Pt in water (right image).[109] Copyright 2004, Royal Chemistry of Society. D) Schematic diagram of the electron transfer from LiNaph to fullerene-functionalized AuNPs.[110] Adapted with permission from the American Chemical Society, Copyright 2019. E) CV curves of Pt/PyC$_{60}$, unsupported Pt nanoflakes, and JM Pt/C catalysts in E) 0.5 M H_2SO_4 and F) 0.5 M H_2SO_4 + 1.0 M MeOH solution. G) Mass activity values and ECSA-normalized activities of all the catalysts at 0.85 V vs. RHE. H) Chronoamperometric curves of Pt/PyC$_{60}$, unsupported Pt nanoflakes, and JM Pt/C catalysts.[114] Copyright 2015, Elsevier. I) TEM and J) HRTEM pictures of Cu(15%)-MFC$_{60}$ nanostructures. K) HRTEM image of the highly ordered mesostructure and L) corresponding SAED pattern for 111 crystallographic plane (inset) of the Cu/Cu_2O mesostructure. M) ORR polarization curves at 1600 rpm in O_2-saturated conditions in 0.1 M KOH and N) number of electron distribution as a function of potential for the Cu-MFC$_{60}$ samples. O) Onset potential obtained for RRDE results from Cu(15%)-MFC$_{60}$ with ring potential polarized at 1.5 V (vs. RHE) and P) apparent number of electrons transferred and peroxide formation.[44] Adapted with permission from Wiley-VCH, Copyright 2020.

exhibited better electrocatalytic properties than MFC$_{60}$ platforms and its counterparts, delivering an onset potential of 0.86 V and a half-wave potential of 0.73 V (Figure 3M,O). As shown in Figure 3N, K–L plots revealed that the ORR process was conducted by a four electron transfer pathway from 0.56–0.66 V (vs. RHE). This was confirmed by a decrease of the H_2O_2 yield at higher ORR potentials (Figure 3P). The high ORR activity of the Cu(15%)–MFC$_{60}$ heterostructure was ascribed to both the synergistic contribution from the porous network of fullerenes and the highly conductive Cu metallic domains, improving both the electrocatalytic active surface area and the mass transport processes, therefore shortening the length of the ion diffusion channels and enhancing the overall electrochemical yield. This work showed the synergy between non-precious nanoparticles and mesoporous fullerene nanostructured frameworks for the efficient electroreduction of oxygen, thus providing an easy and low-cost strategy to build very active 0D–0D ORR electrocatalysts.

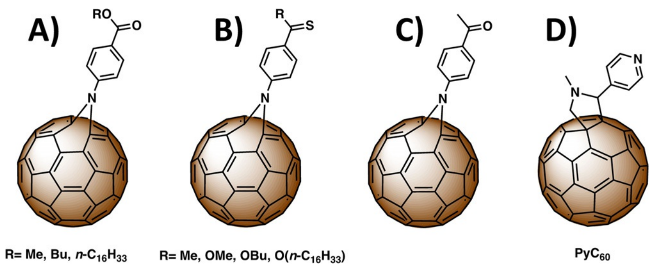

Figure 4. Schematic illustration of A–C) thioketone-substituted aza-homo-[60]fullerenes derivatives. D) PyC$_{60}$, used in catalysis.

3. Fullerene–1D Nanomaterial Hybrids

SWCNTs are particularly promising materials with remarkable applications in electronics and catalysis because of their unique physical and (opto)electronic properties such as high charge mobility, small capacitance, nanoscale size, and high current-carrying capability.[117] Their applications have been extensively studied and several approaches have been used to improve their overall performance. One of the methodologies that has gained more attention is the formation of hybrid materials. In this section, we will discuss the synthesis and properties of fullerene–SWCNT (0D–1D) hybrid materials.

3.1. Synthesis and Electronic Properties

3.1.1. C_{60}–CNT Heterostructures with vdW Interactions

Extensive work has been published that describes hybrids of C_{60}–SWCNTs based on vdW interactions.[118–121] One of the most recent articles published in 2019 by Dai et al. shows the adsorption of C_{60} onto the external walls of SWCNTs to prepare trifunctional catalysts used for ORR, oxygen evolution reaction (OER), and hydrogen evolution reaction (HER) over a wide range of pH values.[47] The synthetic process was a simple adsorption method in which the SWCNTs were simply dispersed in a C_{60} aqueous solution. Characterization by Raman Spectroscopy revealed that the nanotube structures became slightly disordered as an intramolecular electron transfer occurred from the SWCNTs to the fullerenes. The X-ray diffraction (XRD) patterns confirmed the high crystallinity of the hybrids, a further indication of the relatively efficient charge mobility and electrochemical stability.

It has been shown that the interaction of some fullerene derivatives with SWCNTs can be stronger than that of C_{60}-SWCNTs. As demonstrated by Maggini and co-workers, a C_{60}–pyrene dyad can increase the solubility and facilitate the π–π interactions with SWCNTs compared to pure C_{60}.[122] The synthesis of the C_{60}–pyrene derivative was performed by a reported protocol in which a regioselective Bingel reaction is performed with a tether–pyrene addend to obtain a *cis*-2-C_{60}-bisadduct (Figure 5 A).[123] The synthesis of the hybrid was carried out by preparing a mixture of SWCNTs and the C_{60} derivatives in DMF or THF and stirring it for 24 hours. The mixture was then ultrasonicated and centrifuged to collect the products.

3.1.2. Fullerene–SWCNT Peapods

0D–1D hybrid materials are not only limited to those prepared via the physical adsorption to the external walls of the carbon nanotubes (CNTs), in fact, the so-called fullerene–SWCNT peapods have been extensively studied throughout the years. These materials were first discovered in 1998 by serendipity,[124] and since then, they have attracted considerable attention because of their unique properties when compared to their pure counterparts. The introduction of fullerenes into SWCNTs can significantly alter the electronic structure of the surrounding CNT, leading to pronounced modifications to the band gap and unoccupied density of states.[125] The synthetic methods used to prepare these 0D–1D nanocomposites include gas-phase reactions, temperature-shock treatment, heating at temperatures close to sublimation,[126] as well as arc discharge methods.[127] Besides C_{60}, there are many other examples, including metallofullerenes, that have also been incorporated inside SWCNTs, such as C_{70}, C_{78}, C_{80}, C_{84}, $Sc_3N@C_{80}$, $Dy_3N@C_{80}$, $Gd@C_{82}$, $La_2@C_{80}$, $Ti_2@C_{80}$, and $Ce@C_{82}$ (Figure 5 B,C).[126–128] It has been shown that the fullerene inside the SWCNT exhibits free rotation which can influence its physical and electronic properties (Figure 5 C).[127]

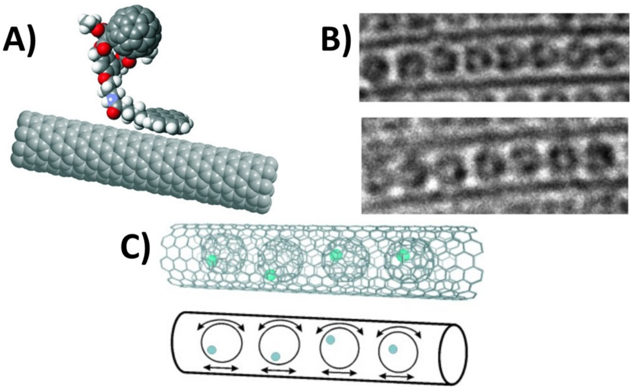

Figure 5. A) Semiempirical (PM3) optimized geometry of C_{60}–pyrene conjugate in the presence of a (9,0) SWCNT.[122] Copyright 2006, Wiley-VCH. B) HRTEM micrographs of a bundle of $(Ce@C_{82})@SWCNT$ structures taken with 2 and 1 s camera exposures. C) Translational oscillations and discontinuous molecular rotations observed for $Ce@C_{82}$.[127] Copyright 2004, Wiley-VCH.

Interesting articles have been published regarding the syntheses and properties of peapods. Mizutani et al. prepared a doped metallofullerene–SWCNT peapod containing $Gd@C_{82}$, which exhibited ambipolar transistor behavior.[129] By incorporating an endohedral fullerene within the SWCNT, there was a notable narrowing of the observed band gap from 0.5 to 0.1 eV. In addition to its field-effect transistor (FET) properties, the 0D–1D hybrid had the capability of acting as both an n- or p-type semiconductor. These results constituted a significant improvement since usually the semiconducting properties of C_{60}-peapod-FETs and SWNTs–FETs tend to exhibit only p-type semiconductor behavior. The metallofullerenes can be considered as unique building blocks within the 0D–1D heterostructures since they can act as small individual circuits that can be finely tuned. The results revealed a significant decrease in current by an estimated three orders of magnitude (approximately 0.06 to 0 nA), followed by a sudden spike near 0.35 nA.

To the best of our knowledge, there are no articles that report the catalytic activity of peapods for HER or ORR, so this remains as a potentially open and exciting avenue to explore.

3.1.3. C_{60}–CNT Heterostructures Linked Covalently

There are numerous reports of covalent attachment of fullerenes to SWCNTs.[130–133] In an article published in 2007 by Langa et al.,[130] a simple amidation of an acid-functionalized SWCNT was performed to obtain the 0D–1D nanohybrid with the fullerene attached to the ends of the SWCNT. The structures were confirmed using high-resolution transmission electron microscopy (HRTEM), Fourier-transform infrared spectroscopy (FTIR) and Raman spectroscopy. More recently, Zhang and co-workers reported an interesting comparison study between CB-C_{60}-SWCNT covalently functionalized with 4-chlorobenzoic acid (CB) and a vdW C_{60}–SWCNT hybrid using a two-step synthetic approach.[134] C_{60} was functionalized with CB following a Friedel–Crafts acylation reaction, and then coupled to the SWCNT surfaces using a Birch reduction (Figure 6A). The resulting 0D–1D nanohybrids were washed with CS_2 under ultrasonication to eliminate the physically adsorbed fullerene molecules. The products were characterized by HRTEM and the C_{60} molecules were clearly seen on the CNT surfaces (Figure 6C). According to the XRD patterns, the 0D–1D hybrid formed via vdW interactions exhibited poor crystallinity in comparison to the covalently bonded 0D–1D hybrid. In addition to the improvement in the morphology of the covalently bonded C_{60}–SWCNT hybrid, the latter also exhibited a higher surface area (422.52 $m^2 g^{-1}$) than the vdW C_{60}–SWCNT hybrid (258.5 $m^2 g^{-1}$).

3.2. Catalytic Properties

Within the last decade, hybrids of fullerenes and 1D nanomaterials have been employed for the fabrication of energy-related materials with outstanding light energy harvesting and photovoltaic properties due to their unique extended π-delocalization properties.[118,135–139] Particularly, SWCNT nanohybrids have been well studied. Several synthetic strategies have been used to create diverse types of these assemblies such as vdW assemblies,[136] covalently linked composites,[130] peapods,[140] and more recently the encapsulation and the covalent linkage of endohedral fullerenes to SWCNTs.[141,142] Although in-depth understanding of the photoenergy conversion processes of C_{60}–SWCNT nanohybrids has been achieved,[143,144] their applications for electrocatalysis have been scarcely studied to date. However, their intermolecular charge-transfer properties have recently sparked attention in the fields of materials science and catalysis.

The attachment of fullerenes to the sidewall of SWCNTs by covalent and non-covalent interactions has received a lot of attention as a powerful alternative to build high-perfor-

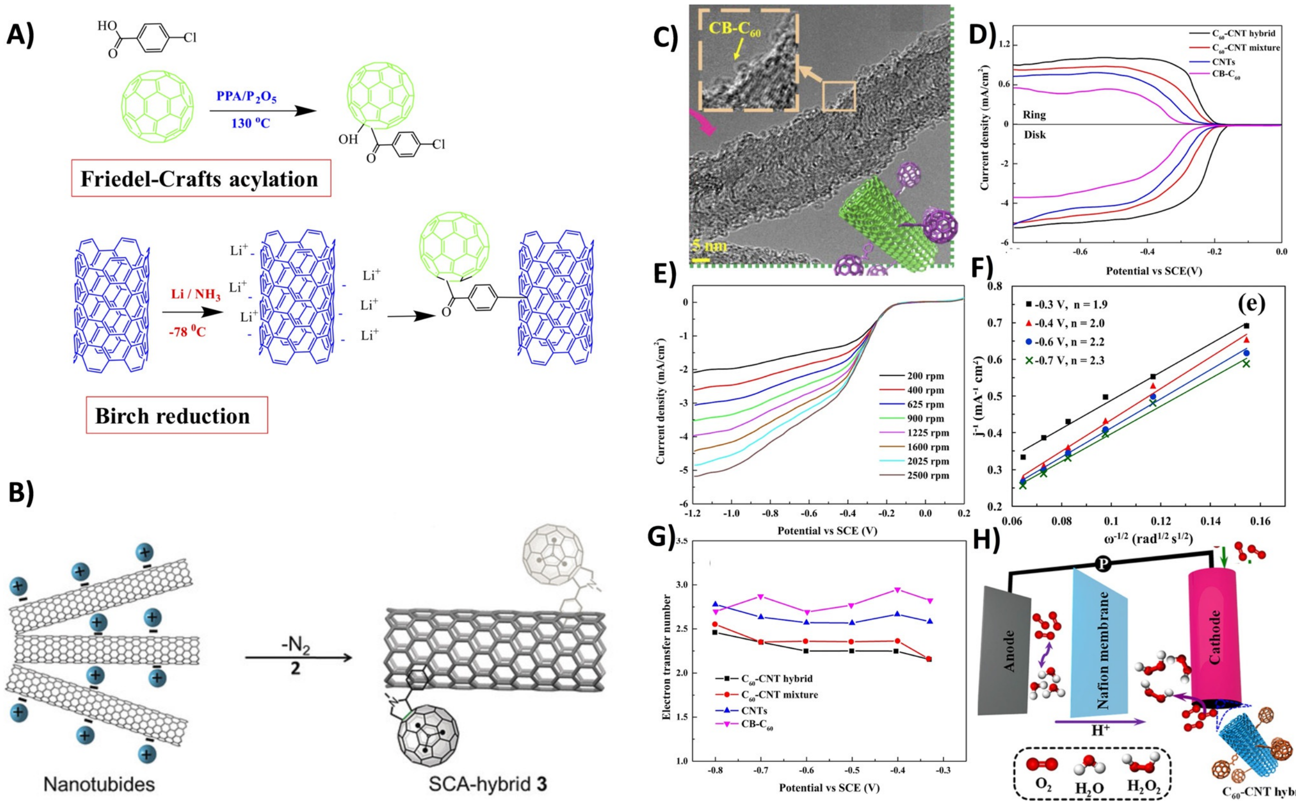

Figure 6. A) Synthetic strategy of CB–C_{60} and C_{60}–CNTs hybrids via covalent attachment. B) Attachment of endohedral $Sc_3N@C_{80}$ to the sidewall of SWCNTs by using negatively charged SWCNTs.[142] Adapted with permission from Wiley-VCH, Copyright 2019. C) TEM image of the C_{60}–CNT heterostructures. D) RRDE polarization curves at 1600 rpm in O_2-saturated and 0.05 M H_2SO_4 of CNTs, CB–C_{60}, and C_{60}–CNTs. Scan rate: 10 $mV s^{-1}$. E) Rotating disk electrode measurements and F) K–L plots of the C_{60}–CNTs at pH 3, scan rate 50 $mV s^{-1}$. G) Electron transfer number as a function of the potential for CNTs, CB–C_{60} and C_{60}–CNTs. H) Schematic illustration of the H_2O_2 production by the C_{60}–CNT hybrid electrode.[145] Adapted with permission from Nature publising group, Copyright 2019.

mance electrocatalysts. Zhang and co-workers have covalently attached C_{60} derivatives on the sidewall of MWCNTs (Figure 6A,C). The C_{60}–CNT hybrids showed excellent performance for the two-electron reduction of oxygen to H_2O_2.[145] As shown in Figure 6D, C_{60}–CNT nanocomposites surpassed the electrocatalytic activities of their components for the generation of hydrogen peroxide yielding a disk current density (J_k) of $-5.3\ \mathrm{mA\,cm^{-2}}$ at -0.4 V (vs. SCE), and the highest hydroperoxy efficiency with a ring current density value of $0.91\ \mathrm{mA\,cm^{-2}}$ at -0.4 V (vs. SCE) and an onset potential of -0.12 (vs. SCE) at 1600 rpm. The number of exchanged electrons for the nanocomposites was very close to two electrons, clearly showing their high selectivity towards hydrogen peroxide formation (Figure 6G). The rotating disk electrode (RDE) and the K–L plots (Figure 6E,F) demonstrated that the nanohybrids followed first-order kinetics for ORR transferring $2.2\,e^-$ per O_2 molecule.

The catalytic activity of the 0D–1D hybrids was comparable to those of state-of-the-art two-electron oxygen reduction carbon-based nanoelectrocatalysts.[146,147] The excellent catalytic performance of the C_{60}–SWCNTs nanohybrids was linked to the carbon nanostructured network, which provides a large number of active sites. The high electron mobility through the fullerene units and the covalent linkage between the C_{60}–CB and the CNTs increase the more favorable adsorption states of the intermediate reactants such as OOH* during ORR reactions. This work has paved the way towards the rational design of 0D–1D nanohybrids composed of CNTs covalently functionalized with fullerenes as promising cathode materials for efficient peroxide generation (Figure 6H). Also, the covalent binding between endohedral $Sc_3N@C_{80}$ and SWCNTs has been recently reported (Figure 6B).[142] The electrocatalytic function of these interesting heterostructures has not been tested to date.

vdW C_{60}-SWCNT nanohybrids with superior electrocatalytic performances for water splitting reactions have been fabricated taking advantage of the efficient intermolecular charge-transfer processes from the CNTs to the fullerene nanocages. Dai and co-workers have reported a new class of trifunctional metal-free electrocatalysts based on C_{60} adsorbed onto SWCNT surfaces using an easy one-step ultrasonication methodology for 5, 10, 15, and 20 minutes.[47] The as-synthesized C_{60}–SWCNT displayed an unprecedented multifunctional pH-universal catalytic activity towards hydrogen evolution, oxygen reduction, and oxygen evolution reactions. In basic environments (0.1 M KOH), the vdW 0D–1D nanohybrids (C_{60}–SWCNT$_{15}$) considerably surpassed the catalytic activity of both SWCNTs and C_{60} for all three reactions (Figure 7A–C). For the OER reaction, the ΔE value ($\eta_{10}-E_{1/2}$) was 0.82 V, which is significantly better than that of

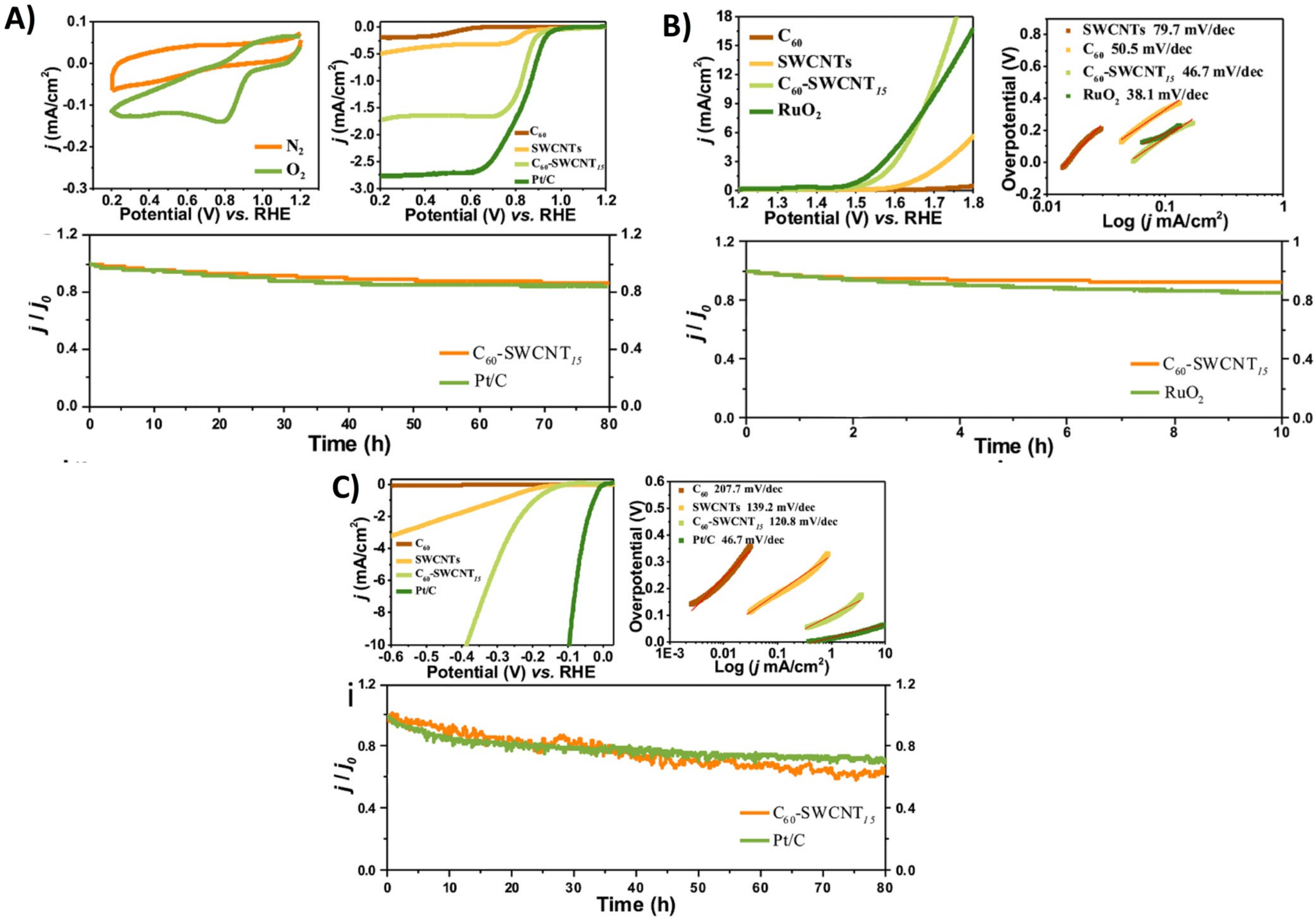

Figure 7. A) HER LSVs, corresponding Tafel plots, and *I*–*t* curves; B) ORR LSVs, corresponding Tafel plots, and *I*–*t* curves; C) OER LSVs, corresponding Tafel plots, and *I*–*t* curves of the vdW C_{60}–SWCNT nanohybrids in a alkaline environment (0.1 M KOH).[47] Adapted with permission from the American Chemical Society, Copyright 2019.

other carbon-free nanoelectrocatalysts including graphene–SWCNTs and g-C_3N_4-carbon.[148,149] C_{60}–SWCNTs$_{15}$ displayed improved ORR and OER electrochemical stability after 80 hours compared to commercial Pt/C in alkaline medium. The aforementioned heterostructures exhibited excellent trifunctional catalytic behavior in both acid and neutral environments.

It is worth noting that the trifunctional electrocatalytic rates of the vdW C_{60}-SWCNT$_{15}$ were markedly linked to the positively charged active sites generated at the C_{60}/SWCNT electrochemical interfaces through the unidirectional intermolecular charge transfer processes from the conductive nanotubes to the strongly electron-accepting fullerene molecules.[150] The positively charged catalytically active sites may modify the binding energies of the reaction intermediates (i.e., OH*, OOH*, O*, and H*) and, in turn, enhance the overall catalytic activity. In summary, these findings provide an in-depth understanding of the nanohybrid catalytic mechanisms and suggest new avenues for the development of inexpensive multifunctional metal-free 0D–1D hybrids with improved catalytic properties.

4. Fullerene–2D Material Hybrids

2D heterostructures are constructed by stacking one or a few monolayers upon one another via vdW interactions. Although the interactions are rather weak, it has been shown that they are adequate to keep the assembled layers together. Various 2D materials have been studied and characterized, including several methods explored to improve their electronic and conducting properties, morphology, crystal packing, and dimensions. In this regard, the formation of hybrids with fullerenes has been one of the most popular approaches amongst many methodologies that have been utilized. For example, heteroatom doping (N, S, B, P, Cl, Br, I) has been used with 0D–2D graphene-fullerene heterostructures to increase the number of active sites. Additionally, other 2D materials have been studied for 0D–2D hybrids such as g-C_3N_4, „white-graphene“ hexagonal boron nitride (HBN), graphene oxide (GO)/reduced graphene oxide (rGO) and transition metal dichalcogenides (MoS_2, WS_2, WSe_2).

4.1. Synthesis and Electronic Properties

4.1.1. C_{60}–Graphene Heterostructures with vdW Interactions

During the last decade, many articles reported the fabrication of C_{60}-graphene heterostructures via vdW interactions[151] for diverse applications such as solar cells,[152] sensors,[153,154] supercapacitors,[155] catalysis,[156,157] and lithium-ion batteries.[158] These 0D–2D hybrids can be synthesized as physical blends or bilayer films, depending on the application desired. Commonly used methods are thermal evaporation deposition,[159–163] spray coating,[164] thermal treatment, ultrasonic treatment,[152–156,165] liquid–liquid interfacial precipitation,[166] and acid treatment.[158]

The overall architecture of the fullerene–graphene 0D–2D hybrids is generally referred to as graphene nanobuds. Owing to the rather weak intermolecular forces and lack of directionality or orientation, vdW interactions tend to exhibit, in this type of 0D–2D hybrids, a relatively compressed packing density. This is consistent with both theoretical and experimental results, further indicating that the C_{60} molecules are „locked“ into the graphene lattice at the interface.[167] However, the dimension of the 0D–2D heterostructure is dictated by stoichiometry, the size of the molecule, and its coverage of the surface material. Further modifications of the 0D–2D hybrid can be made by doping, which can also alter the electrostatic interactions of molecules with the adjacent layer. The introduction of C_{60} results in charge transfer and vdW interactions as a result of the π–π stacking between the molecules and the graphene network. It is precisely this interaction that dictates the packing density of the first few layers, adsorption of the molecules, and the overall 0D–2D heterostructure.

i. Physical blends

One of the most used methods to synthesize 0D–2D fullerene/graphene hybrids is physical blending. This can result in nanomaterials with different morphologies. In 2011, Shin et al. studied the synthesis of a hybrid rGO/C_{60} using a liquid–liquid interfacial precipitation method to yield very well defined nanowires (Figure 8).[166] The assembly of the nanowires was driven by π–π interactions that allowed the graphene oxide sheets to wrap around the C_{60} to form nanostructures with p-type semiconducting behavior.

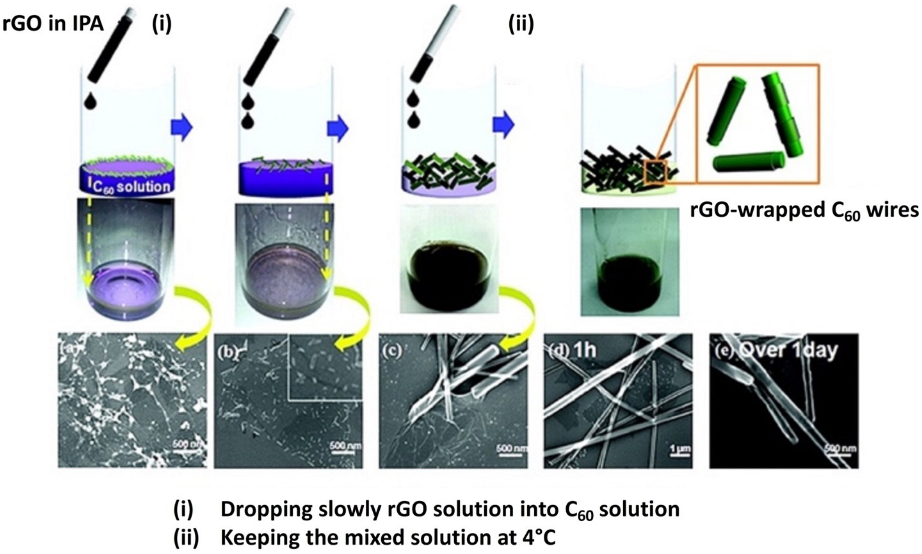

Figure 8. Schematic illustration and SEM images (a–e) showing steps of formation of rGO-wrapped C_{60} wires.[166] Adapted with permission from the American Chemical Society, Copyright 2011.

In the same year, Huang et al. synthesized several hybrids of C_{60}/SWCNT/GO to form water-stable colloidal dispersions. The synthesis was carried out by ultrasonication of the components (C_{60}, SWCNT and as-synthesized GO) to obtain binary and tertiary mixtures. As reported before,[167–172] C_{60} can easily adhere to the surface of graphene by vdW interactions. In these cases, the graphene was functionalized on the surface, thus decreasing its interactions with C_{60}. By using ultrasonication, microcrystals of C_{60} and SWCNT were produced, resulting in a larger surface area and stronger interactions with the surface of the GO. This process allowed the formation of a homogeneous dispersion of components that are usually not soluble or dispersible in water, typically used for photovoltaic applications.

In order to enhance the overlap of π-bonds, the rings of a C_{60} molecule align in a parallel fashion with the surface of graphene (face-on orientation). Kim et al. reported TEM images that confirmed the morphology of graphene–C_{60}, with the fullerene exhibiting a highly ordered „hexagonal honeycomb structure“.[169] Several possibilities for the molecular arrangement of fullerenes at low temperatures in 0D–2D heterostructures were determined to be energetically favorable using computational models. Experimentally, the graphene/C_{60} hybrids show that the C_{60} molecules tend to favor a zigzag and armchair lattice direction along the graphene surface.

Not all of the 0D–2D hybrids featuring fullerenes and GO are fabricated with pristine C_{60} or C_{70}.[172] Qiao et al. recently described a hybrid of GO with multi-functionalized fulleropyrrolidine C_{60} derivatives (PyrC_{60}, see Figure 10A in Section 4.1.2) by a self-assembly process.[173] Similar to previous reports, the GO and the PyrC_{60} were mixed and sonicated in a mixture of ethanol/water to obtain the 0D–2D composites. The authors noticed that by increasing the amount of PyrC_{60} in the mixture, the number of floating particles was reduced until a clear solution was obtained at a ratio of 2:1 (GO/PyrC_{60}).

ii. Bilayers

Another common method to prepare 0D–2D fullerene/GO hybrids is by forming bilayers, typically used for supercapacitors and photovoltaic applications. Generally, the graphene–C_{60} heterostructures are considered an n-type semiconductor that transports electrons in the perpendicular direction to the 2D layers. Several approaches have been made to tailor the interfacial properties of 0D–2D hybrids, specifically, the charge transfer of graphene–C_{60}, which can alter the overall electronic transport of the 0D–2D composites.

Ojeda-Aristizabal et al. analyzed, both experimentally and theoretically, the structure and charge transfer of a hybrid graphene/C_{60}/h-BN.[167] The DFT calculations revealed different molecular arrangements, interfacial band structures, electron–hole mobilities, and intrinsic charge transfer of the stacked C_{60} layers, ultimately dependent on the deposition process of h-BN.

Generally, h-BN is an ideal choice of substrate because of its chemical inertness, however, calculations revealed its significant effect on the 0D–2D hybrid's polarizability and charge transfer. Experimentally, the orientation of C_{60} assumed a „dimer/hole“ configuration, consistent with theoretical studies. In addition to high crystallinity, dependent on the heat applied to the h-BN substrate, the C_{60} molecules were ordered in a triangular patterned lattice that was established by TEM and electron diffraction.

Bao et al. investigated the morphology of C_{60} on a graphene layer, its electronic properties, and its application as vertical transistor.[169] The preparation of the graphene was done by chemical vapor deposition (CVD) on a copper foil. The C_{60} was then thermally evaporated onto the graphene layer (Figure 9A).

Using HRTEM and electron diffraction, they observed an epitaxial relationship between the assembled C_{60} crystals and the graphene lattice, where C_{60} shows a well-organized hexagonal honeycomb lattice structure (Figure 9B–D). Ab initio simulations were performed to explain the observed experimental patterns. In the calculations, vdW forces were employed as the primary form of interaction and the results suggest that the latter has a very strong influence in the interfacial junction between C_{60} and graphene (Figure 9E–I).

The bilayer strategy to form fullerene–graphene hybrids is extremely versatile, as demonstrated by Meyer et al., who published the first evidence of C_{60} sandwiched within graphene.[161] The sandwiches were constructed by thermal evaporation and the study revealed that the C_{60} lattice spacing is smaller than expected with a value of 9.6 ± 0.1 Å, indicating that the interaction with the graphene sheets compresses the C_{60} lattice. An interesting finding was that the C_{60} molecules were extremely mobile at the edges of the monolayer, which was observed by HRTEM. To explain this, simulations were performed to calculate the relevant diffusion barriers using the nudged elastic band method. As a result, the authors found that the individual C_{60} molecules can undergo dimer formation and this transition suppresses rotation and locks them into place, allowing their internal structure to be revealed. Overall, the C_{60}–graphene heterostructure provided a nanoscale reaction chamber, some suppression of radiation damage, and a low-contrast background that can be subtracted from the image.

4.1.2. C_{60}–Graphene Heterostructures Linked Covalently

Although noncovalent 0D–2D hybrids have been extensively explored, optimization of their structures and properties has proven to be difficult. In order to improve their properties, covalent functionalization has also been utilized as an alternative approach.

The first directly bonded C_{60}–graphene hybrid was synthesized by Yang et al. in 2015 using a solid-state mechanochemical method by ball milling with LiOH as the catalyst.[174] After a series of morphological and spectroscopic characterizations, the successful covalent attachment of C_{60} onto the edges of the graphene nanoplatelets was confirmed. A mechanism of formation was proposed involving two critical steps: the generation of a reactive carbon species (radicals and ions) induced by the catalyst LiOH and the reaction between the reactive carbon species and gaseous or solid reactants introduced into the sealed ball-mill crusher to bond C_{60} onto the edge of the graphene via two C−C single

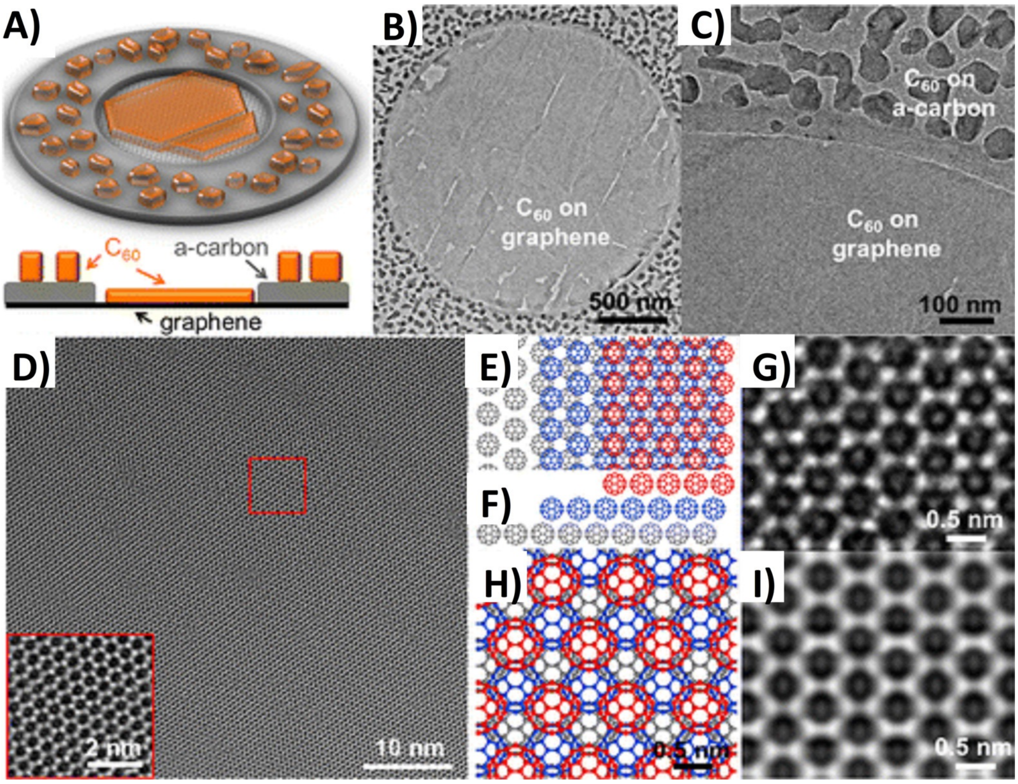

Figure 9. C$_{60}$ thin film grown on graphene. A) Schematic of C$_{60}$ film grown on a graphene membrane. C$_{60}$ is thermally evaporated onto a graphene TEM grid. The central circular region has a suspended graphene membrane. Outside the circle, the C$_{60}$ is evaporated onto an amorphous carbon film. The bottom image shows a side view of the sample geometry. B) TEM image of the C$_{60}$ film (10 nm thickness) on graphene. C$_{60}$ uniformly covers the graphene surface. C) TEM image of C$_{60}$ film around the edge of a hole in a Quantifoil TEM grid. The C$_{60}$ morphology on amorphous carbon shows island growth. D) Zoomed-in TEM image of C$_{60}$ film on a graphene membrane. The uniform lattice structure of C$_{60}$ is visible. The red square is a field view for the inset, which clearly shows the crystal structure of the C$_{60}$ thin film. E) Schematic of the C$_{60}$ crystal model with three C$_{60}$ close-packed layers. The three layers (red, blue, and gray) of C$_{60}$ have an ABC stacking relation. F) Side view of the C$_{60}$ model shown in panel (E). G) Atomic resolution TEM image of a C$_{60}$ crystal grown on graphene. H) C$_{60}$ crystal model with three layers. I) TEM simulation image of model (H).[169]Copyright 2015, American Chemical Society.

bonds. Raman spectroscopy showed a significantly high I_D/I_G ratio (0.40), which can be attributed to distortion of the graphene because of the reduced grain size, which was consistent with SEM images that showed the hybrid's overall homogeneous morphology and the observed distortions in the graphene layers. TEM images exhibited approximately five distorted graphene layers in the synthesized 0D–2D hybrid. In addition, an increase in surface area (211.3 $m^2 g^{-1}$), in comparison to pristine graphite (2.8 $m^2 g^{-1}$), was observed.

Similarly, Chen et al. reported a graphene–C$_{60}$ hybrid material using a chemical coupling method between graphene oxide and fulleropyrrolidine derivatives (Figure 10 A,B).[175] In this case, the synthesis method used was completely different. Pyrrolidine–C$_{60}$ derivatives were synthesized by a photochemical reaction between C$_{60}$ and amine acid esters and further attached to the acyl-chloride-functionalized GO by a condensation reaction. The successful attachment was confirmed by FTIR and Raman spectroscopy, thermogravimetric analysis (TGA), X-ray photoelectron spectroscopy (XPS), and HRTEM.

4.2. Catalytic Properties

i. Water splitting properties

Two-dimensional materials have been recently coupled to a large number of LD nanostructures such as quantum dots, nanoparticles and nanowires to construct high-efficiency nanohybrid electrocatalysts for water splitting reactions.[176,177] The possibility to tune their physicochemical properties by surface chemical modification or defect engineering has opened up attractive strategies for the development of new classes of heterostructures with outstanding electrocatalytic performances. Fullerenes are excellent candidates to modify the electronic structures of 2D materials to extend their functionalities and, in turn, their energy-related applications.[36] Although the development of fullerene–2D nanomaterial hybrids for electrocatalytic reactions is still in its infancy, seminal examples have shown the high potential of these nanoassemblies for water splitting reactions.[36] Both functionalized fullerenes and fullerene-derived nanostructures have been used as efficient building blocks to form high-performance electrocatalysts. The fabrication of QDs from C$_{60}$ molecules has sparked an interest for electrocatalysis.[41] Wang et al. recently reported non-precious electrocatalytic materials by assembling fullerene quantum dots decorated with CoNi layered nanosheets onto Ni foam (NF) electrodes (FQD/CoNi-LDH/NF) through a simple one-pot hydrothermal strategy.[43] The nanohybrid materials exhibited excellent yields for OER with lower overpotentials at a current density of 50, 100, and 200 $mA\,cm^{-2}$ than both their components and commercial IrO$_2$ deposited on NF (Figure 11 A). Additionally, the nanoheterostructures delivered superior HER catalytic activity compared with their components (Figure 11 B), exhibiting lower Gibbs free energies for hydrogen absorption. The increased catalytic activity was linked to the intermolecular charge transfer between the fullerene quantum dots and the CoNi nanosheets, which indeed decrease the energy barriers for the formation of intermediate catalytic species. Bearing in

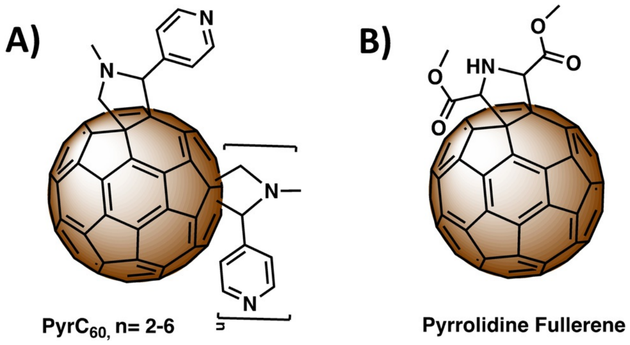

Figure 10. Fullerene derivatives used to form 0D–2D heterostructures.

mind their extraordinary HER and OER properties, the hybrids were tested as anode and cathode materials for water splitting and they generated a current density of 10 mA cm^{-2} at 1.59 V (Figure 11 D), which is similar to the values for state-of-the-art 2D nanomaterials. This work sheds light on the effect of fullerene quantum dots over the catalytic activity of nanostructured hybrids and paves the way towards the development of non-noble multifunctional 0D–2D electrocatalysts for practical applications in the construction of efficient water splitting devices.

Other types of 0D–2D electrocatalytic composites have been assembled. Graphene nanoplatelets and C_{60} molecules were covalently bonded using LiOH as a catalyst via a solid-state mechanochemical strategy (Figure 11 C).[178] The graphene–C_{60} hybrids largely outperformed the ORR catalytic activity of the pristine graphene and C_{60} (Figure 11 E,F). The charge transfer processes from the graphene to the C_{60} molecules induce a net positive charge on the graphene basal planes giving rise to highly active catalytic sites. The aforementioned results demonstrated that the pronounced electron-acceptor properties of fullerenes adsorbed on 2D nanostructures can promote an efficient intermolecular electron transfer from the nanosheets to the C_{60} molecules, which, in turn, triggers the formation of new types of electrocatalytic active sites for the HER and OER processes.

Fullerene-modified molybdenum disulfide (MoS_2) nanostructures have also been explored as water-splitting catalysts. C_{60} nanoclusters (nC_{60}) have been integrated into MoS_2/carbon fiber paper (CFP) architectures to create highly effective HER electrocatalysts.[45] The HER properties of the fullerene–2D heterostructures were superior to those of the C_{60} and of the 3D MoS_2/CFP, showing an overpotential η_{10} value of 172 mV and a Tafel slope of 60 mV dec^{-1} for the optimized C_{60} loading of 0.5 mg mL^{-1} (Figure 11 G,H). Furthermore, the values of C_{dl} and ECSA were plotted as

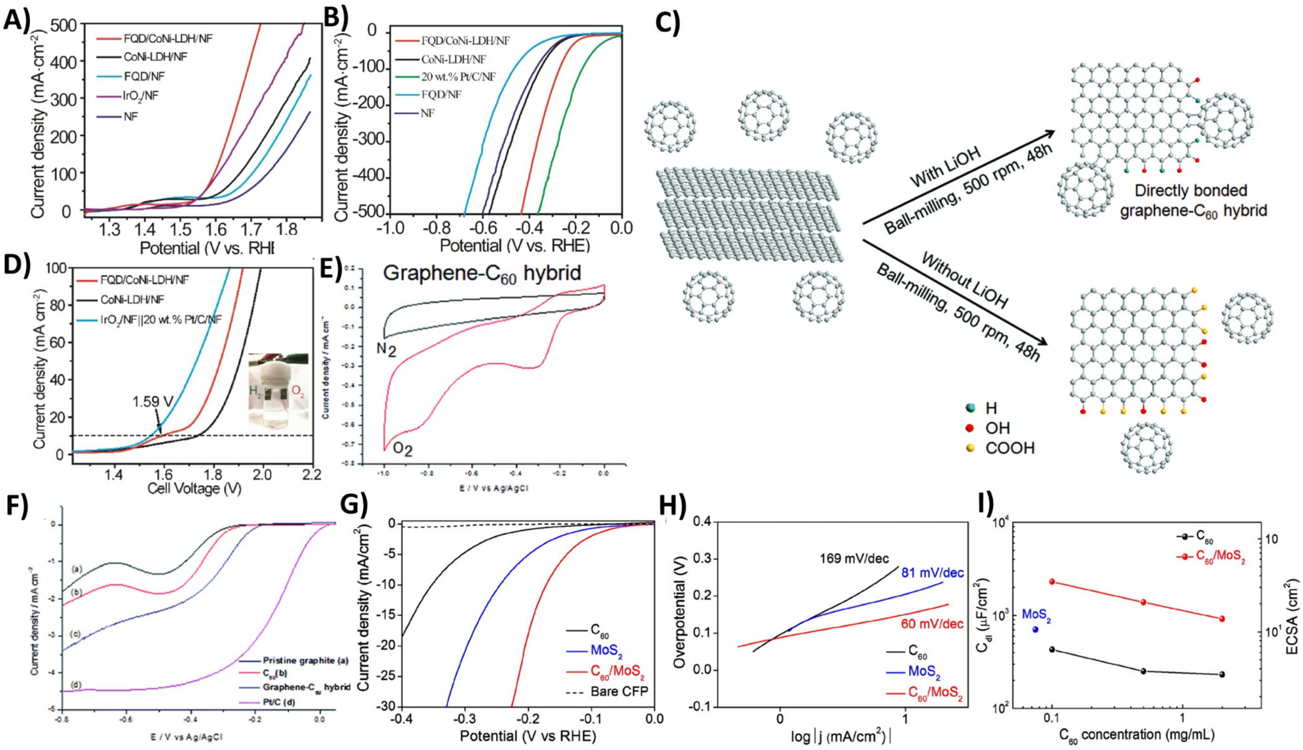

Figure 11. A) HER and B) OER polarization curves of the FQD/CoNi-LDH/NF. C) Schematic diagram of the mechanochemical reaction between graphite and C_{60} molecules. D) LSVs of the water splitting electrolyzer cells of FQD/CoNi-LDH/NF, CoNi-LDH/NF, and IrO_2/NF ‖ 20 wt % Pt/C/NF electrodes in 1 M KOH.[43] Copyright 2020, Elsevier. E) Cyclic voltammograms (CVs) of the graphene–C_{60} heterostructures in N_2- and O_2-saturated 0.1 M KOH. Scan rate: 50 mV s^{-1}. F) ORR polarization curves of pristine graphite, C_{60}, and graphene–C_{60} nanohybrids in 0.1 M KOH at 1600 rpm. Scan rate: 10 mV s^{-1}.[178] Copyright 2015, Royal Society of Chemistry. G) Polarization HER curves and H) corresponding Tafel plots for nC_{60} (0.5 mg mL^{-1}), as-prepared 3D MoS_2 nanosheets, and hybrid nC_{60} (0.5 mg mL^{-1})/MoS_2 architectures deposited on CFP. I) Double layer capacitance as a function of the C_{60} concentration for nC_{60} on CFP (black), 3D nanosheets of MoS_2 (blue), and hybrid nC_{60}/MoS_2 prepared on CFP.[45] Copyright 2016, American Chemical Society.

a function of the C_{60} concentration for the nanohybrids and their components (Figure 11 I). The results revealed the higher number of catalytic active sites for the 0D–2D nanoheterostructures for all concentrations, thus confirming their superior HER performances. The improved catalytic performance was ascribed to the charge transfer from the nC_{60} to the MoS_2, which polarizes the Mo–S bonds, thus decreasing the adsorption energy for the hydrogen cations. In this work, the concept of interfacial doping to improve the electrocatalytic rates of 2D nanomaterials was presented, opening new avenues for the development of 0D–2D nanohybrids with superior catalytic properties.

ii. Photocatalytic properties

The development of (photo)electrocatalytic nanohybrid systems based on low-dimensional materials has attracted considerable interest because of their impressive advantages, including the strong interfacial interactions between their components, high surface area, and desirable band potential, among others.[175,179,180] In addition to having the ability to effectively form a wide range of supramolecular assemblies, fullerenes show remarkable optical and physical properties which makes them excellent candidates to construct photocatalytic LD nanosystems.[37] Their 0D closed-cage molecular structure and high symmetry fulfill an essential role in several (photo)electrocatalytic reactions, improving the quantum efficiency of the overall processes. Fullerenes exhibit a very large band gap which allows them to absorb over the visible and ultraviolet spectral regions. Fullerene functionalization has been employed as a useful strategy to regulate their electronic structures and to significantly boost their (photo)-electrocatalytic performances.[181]

Despite all of these advantages, there are few examples of fullerene-based LD nanoheterostructures for (photo)electrocatalytic applications. Most examples are based on fullerene–2D hybrids.

vdW MoS_2–C_{60} heterostructures have been prepared using a one-pot mechanochemical strategy for the efficient photocatalytic generation of hydrogen.[182] Bulk MoS_2 and C_{60} molecules were mixed with different weight ratios to optimize the photocatalytic hydrogen production process. The resulting 0D–2D nanocomposites were fully characterized by electronic microscopic techniques (Figure 12 A–C). The HRTEM image of MoS_2-C_{60}-BM3, which corresponds to the 1:1 weight ratio, shows the formation of the 0D–2D nanocomposites with the typical MoS_2 fringe lattice distance of 0.62 nm (Figure 12 C). Raman spectra of the heterostructures and their counterparts show a clear downshift in the frequency of the $A_2(2)$ mode of C_{60}, suggesting that an intermolecular charge transfer process from MoS_2 to C_{60} is taking place (Figure 12 D). The photocatalytic hydrogen production rates were determined for the nanocomposites as well as for the pristine MoS_2 and C_{60} after a ball milling process. The MoS_2-C_{60}-BM3

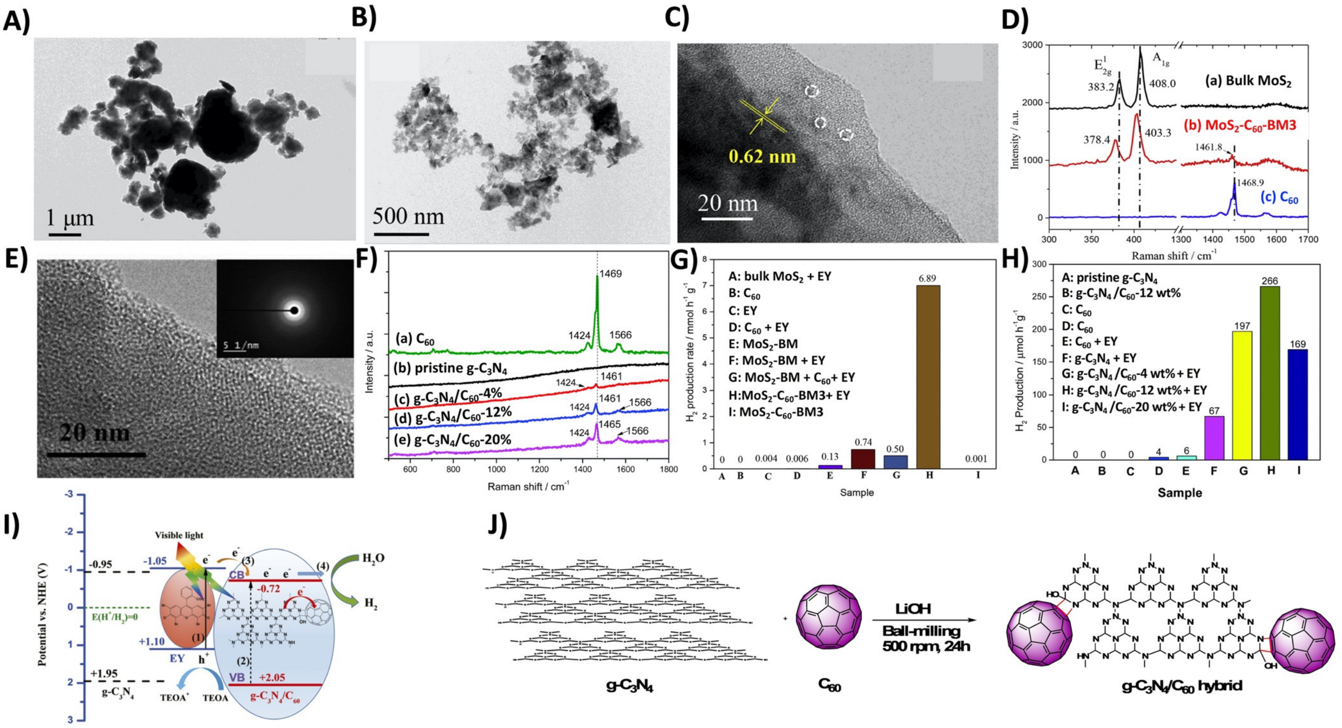

Figure 12. TEM images of A) MoS_2-BM and B) MoS_2-C_{60}-BM3 nanohybrids. C) HRTEM of MoS_2-C_{60}-BM3. D) Raman spectra of the bulk MoS_2, MoS_2-C_{60}-BM3 nanohybrid, and C_{60} powder.[182] Adapted with permission from Elsevier, Copyright 2018. E) HRTEM and F) Raman spectroscopy of the g-C_3N_4/C_{60} 12 wt% nanohybrid.[185] Adapted with permission from the Royal Chemical Society, Copyright 2017. G) Photocatalytic yields of the MoS_2-C_{60}-BM3 0D–2D composites for hydrogen production.[182] Adapted with permission from Elsevier, Copyright 2018. H) Photocatalytic yields for the hydrogen generation of the as-synthesized g-C_3N_4/C_{60} nanohybrids in 5 vol% TEOA aqueous solution in the presence of EY for 3 h under visible light ($\lambda > 420$ nm) irradiation of a 300 W Xe lamp. I) Scheme of the photocatalytic hydrogen production mechanism for the g-C_3N_4/C_{60} nanohybrids. J) Schematic representation of the mechanochemical reaction between g-C_3N_4 and C_{60} in the presence of the LiOH catalyst.[185] Reproduced with permission from the Royal Chemical Society, Copyright 2017.

nanohybrids perform better than the other materials with the highest hydrogen production rate of 6.89 $\mathrm{mmol\,h^{-1}\,g^{-1}}$ (Figure 12G). The enhanced (photo)electrocatalytic activity of vdW MoS_2-C_{60}-BM3 was explained on the basis that fullerenes lead to faster photoinduced electron transfer processes which, in turn, significantly decrease the number of electron–hole recombinations, thus improving the overall (photo)electrocatalytic efficiency. Fullerene functionalization induces a partial exfoliation of the MoS_2 layers that creates more catalytic sites in the 0D–2D material. This work provides new insights into the hybridization of 2D MoS_2 and C_{60} via vdW interactions to facilitate the (photo)electrocatalytic generation of molecular hydrogen.

Graphitic carbon nitride is an emerging 2D nanomaterial that has been employed to create efficient photocatalytic water splitting nanosystems.[183,184] g-C_3N_4 usually displays poor electrical conductivity and low photocatalytic activity because of the rapid recombination of photogenerated electron–hole pairs. For this reason, improving the photocatalytic activity of these 2D platforms is highly desired. To improve their photophysical properties, fullerenes have been covalently attached to their 2D structures using mechanochemistry. Yang and co-workers have synthesized a covalently bonded g-C_3N_4-fullerene 0D–2D nanohybrid using a solid-state mechanochemical strategy in the presence of lithium hydroxide (LiOH) as a catalyst, changing the weight ratio of g-C_3N_4 and C_{60} (Figure 12J).[185] HRTEM and Raman spectroscopy demonstrated the covalent anchorage of the C_{60} molecules onto the 2D g-C_3N_4 layers (Figure 12E,F). The 0D–2D heterostructure showed improved (photo)electrocatalytic properties, delivering an H_2 production rate of 266 $\mathrm{\mu mol\,h^{-1}\,g^{-1}}$ in a noble-metal-free configuration, which is around 4.0 times higher than that obtained for the pristine g-C_3N_4 (Figure 12H). The improved photocatalytic activity was directly linked to the ability of the fullerenes to drastically decrease the conduction band of g-C_3N_4, thus hindering the hole–electron pair recombination processes (Figure 12I).

5. Conclusions and Perspectives

Recently, the assembly of fullerenes and LD nanostructures to create nanoheterostructures for improved electrocatalytic and photocatalytic properties has shown great potential for water splitting, methanol electrooxidation, and photocatalytic generation of hydrogen. Herein we describe the synthetic strategies, structural properties, electrocatalytic and photocatalytic performances, as well as the role of the fullerenes and the catalytic mechanisms of these nanohybrid structures. Despite the progress that has been made, the development of advanced fullerene-based low-dimensional (photo)electrocatalysis is still at an early stage and more details about the underlying catalytic mechanisms need to be disentangled.

Most fullerene nanohybrids undergo structural changes during the catalytic reactions, which significantly influence their overall catalytic yields. The absence of in situ/operando characterization techniques strongly limits the identification of both the catalytic active sites and the intermediate reactants of the electrocatalytic reactions, which limits the understanding of the underlying catalytic pathways. The study of the catalytic reactions with a combination of different advanced in situ/operando characterization techniques, such as FTIR, XPS, Raman infrared, and TEM spectroscopy, will facilitate the rational design of advanced fullerene-based electrocatalysts. They can provide in-depth information about the evolution of the interfacial, chemical, and electronic states as a function of the applied potential of these heterostructures.

Bearing in mind the recent promising theoretical results about their exciting catalytic properties, endohedral fullerenes are strong candidates for efficient nanoheterostructures with improved electrocatalytic properties. Their ability to drastically decrease the Gibbs free energy values for hydrogen adsorption could be combined with the excellent conductive properties of 1D CNTs or 2D ultrathin nanosheets, such as graphene, g-C_3N_4, hexagonal boron nitride, or MXenes, to develop highly efficient water splitting systems. The resulting nanohybrids could also be used as a new generation of NRR catalysts and open a new chapter in the field of electrocatalysis. Transfer of electrons from metallic clusters to the carbon atoms of the nanocages could further increase their electrocatalytic rates, resulting in new catalysts with unprecedented properties.

A set of more realistic computational methods needs to be developed to obtain a better understanding of the fundamental relationship between the electronic structures and the catalytic function of the fullerene-based low-dimensional materials at the atomic scale. Simplified theoretical models usually don't reproduce the experimental conditions very well. Consequently, new simulations are needed for constructing both fullerene-based electrocatalysts and fullerene-based photocatalysts with superior performances.

Undoubtedly, fullerene-based low-dimensional nanosystems will continue to impact both materials science and catalysis in many ways because of their attractive and desirable properties for the development of high-performance catalysts.

Acknowledgements

We would like to thank the US National Science Foundation (NSF) for the generous support of this work under CHE-1801317 (to L.E.). The Robert A. Welch Foundation is also gratefully acknowledged for an endowed chair to L.E. (grant AH-0033).

Conflict of interest

The authors declare no conflict of interest.

---

[1] X. K. Kong, Z. M. Peng, *Mater. Today Chem.* **2019**, *11*, 119–132.

[2] J. Di, C. Yan, A. D. Handoko, Z. W. Seh, H. M. Li, Z. Liu, *Mater. Today* **2018**, *21*, 749 – 770.
[3] X. Y. Chia, M. Pumera, *Nat. Catal.* **2018**, *1*, 909 – 921.
[4] P. Z. Chen, Y. Tong, C. Z. Wu, Y. Xie, *Acc. Chem. Res.* **2018**, *51*, 2857 – 2866.
[5] J. Li, G. F. Zheng, *Adv. Sci.* **2017**, *4*, 1600380.
[6] H. C. Tao, Y. A. Gao, N. Talreja, F. Guo, J. Texter, C. Yan, Z. Y. Sun, *J. Mater. Chem. A* **2017**, *5*, 7257 – 7284.
[7] H. Y. Jin, C. X. Guo, X. Liu, J. L. Liu, A. Vasileff, Y. Jiao, Y. Zheng, S. Z. Qiao, *Chem. Rev.* **2018**, *118*, 6337 – 6408.
[8] Y. W. Liu, C. Xiao, P. C. Huang, M. Cheng, Y. Xie, *Chem* **2018**, *4*, 1263 – 1283.
[9] L. Men, M. A. White, H. Andaraarachchi, B. A. Rosales, J. Vela, *Chem. Mater.* **2017**, *29*, 168 – 175.
[10] G. Hyun, S. Park, J. Jeong, K. S. Lee, D. I. Son, H. Lee, Y. Yi, *J. Phys. Chem. C* **2017**, *121*, 12230 – 12235.
[11] Y. Pan, K. A. Sun, Y. Lin, X. Cao, Y. S. Cheng, S. J. Liu, L. Y. Zeng, W. C. Cheong, D. Zhao, K. L. Wu, Z. Liu, Y. Q. Liu, D. S. Wang, Q. Peng, C. Chen, Y. D. Li, *Nano Energy* **2019**, *56*, 411 – 419.
[12] X. C. Du, J. W. Huang, J. J. Zhang, Y. C. Yan, C. Y. Wu, Y. Hu, C. Y. Yan, T. Y. Lei, W. Chen, C. Fan, J. Xiong, *Angew. Chem. Int. Ed.* **2019**, *58*, 4484 – 4502; *Angew. Chem.* **2019**, *131*, 4532 – 4551.
[13] Z. H. Xia, S. J. Guo, *Chem. Soc. Rev.* **2019**, *48*, 3265 – 3278.
[14] A. Nilsson, L. G. M. Pettersson, B. Hammer, T. Bligaard, C. H. Christensen, J. K. Norskov, *Catal. Lett.* **2005**, *100*, 111 – 114.
[15] J. J. Song, C. Wei, Z. F. Huang, C. T. Liu, L. Zeng, X. Wang, Z. C. J. Xu, *Chem. Soc. Rev.* **2020**, *49*, 2196 – 2214.
[16] M. C. Luo, S. J. Guo, *Nat. Rev. Mater.* **2017**, *2*, 17059.
[17] Y. Zhou, Z. Z. Zhou, R. X. Shen, R. G. Ma, Q. Liu, G. Z. Cao, J. C. Wang, *Energy Storage Mater.* **2018**, *13*, 189 – 198.
[18] Y. Jiao, Y. Zheng, M. T. Jaroniec, S. Z. Qiao, *Chem. Soc. Rev.* **2015**, *44*, 2060 – 2086.
[19] P. Y. Kuang, M. He, B. C. Zhu, J. G. Yu, K. Fan, M. Jaroniec, *J. Catal.* **2019**, *375*, 8 – 20.
[20] T. A. Shifa, F. M. Wang, Y. Liu, J. He, *Adv. Mater.* **2019**, *31*, 1804828.
[21] J. H. Peng, X. Z. Chen, W. J. Ong, X. J. Zhao, N. Li, *Chem* **2019**, *5*, 18 – 50.
[22] Q. S. Gao, W. B. Zhang, Z. P. Shi, L. C. Yang, Y. Tang, *Adv. Mater.* **2019**, *31*, 1802880.
[23] H. F. Wang, C. Tang, Q. Zhang, *Nano Today* **2019**, *25*, 27 – 37.
[24] J. H. Bang, P. V. Kamat, *ACS Nano* **2011**, *5*, 9421 – 9427.
[25] D. Voiry, H. S. Shin, K. P. Loh, M. Chhowalla, *Nat. Rev. Chem.* **2018**, *2*, 0105.
[26] Z. Z. Luo, Y. Zhang, C. H. Zhang, H. T. Tan, Z. Li, A. Abutaha, X. L. Wu, Q. H. Xiong, K. A. Khor, K. Hippalgaonkar, J. W. Xu, H. H. Hng, Q. Y. Yan, *Adv. Energy Mater.* **2017**, *7*, 1601285.
[27] C. Z. Zhu, Y. T. Wang, Z. F. Jiang, F. C. Xu, Q. M. Xian, C. Sun, Q. Tong, W. X. Zou, X. G. Duan, S. B. Wang, *Appl. Catal. B* **2019**, *259*, 118072.
[28] J. Zhang, T. Wang, D. Pohl, B. Rellinghaus, R. H. Dong, S. H. Liu, X. D. Zhuang, X. L. Feng, *Angew. Chem. Int. Ed.* **2016**, *55*, 6702 – 6707; *Angew. Chem.* **2016**, *128*, 6814 – 6819.
[29] X. J. She, J. J. Wu, H. Xu, J. Zhong, Y. Wang, Y. H. Song, K. Q. Nie, Y. Liu, Y. C. Yang, M. T. F. Rodrigues, R. Vajtai, J. Lou, D. L. Du, H. M. Li, P. M. Ajayan, *Adv. Energy Mater.* **2017**, *7*, 1700025 – 1700031.
[30] F. Navarro-Pardo, J. B. Liu, O. Abdelkarim, G. S. Selopal, A. Yurtsever, A. C. Tavares, H. G. Zhao, Z. M. M. Wang, F. Rosei, *Adv. Funct. Mater.* **2020**, *30*, 1908467.
[31] C. Tang, Q. Zhang, *Adv. Mater.* **2017**, *29*, 1604103.
[32] Z. H. Wen, S. M. Cui, H. H. Pu, S. Mao, K. H. Yu, X. L. Feng, J. H. Chen, *Adv. Mater.* **2011**, *23*, 5445 – 5450.
[33] M. Shakeel, M. Arif, G. Yasin, B. S. Li, H. D. Khan, *Appl. Catal. B* **2019**, *242*, 485 – 498.
[34] L. J. Yang, J. L. Shui, L. Du, Y. Y. Shao, J. Liu, L. M. Dai, Z. Hu, *Adv. Mater.* **2019**, *31*, 1804799.
[35] Y. Yao, Z. W. Jin, Y. H. Chen, Z. F. Gao, J. Q. Yan, H. B. Liu, J. Z. Wang, Y. L. Li, S. Z. Liu, *Carbon* **2018**, *129*, 228 – 235.
[36] M. Q. Chen, R. N. Guan, S. F. Yang, *Adv. Sci.* **2019**, *6*, 1800941.
[37] Y. Pan, X. J. Liu, W. Zhang, Z. F. Liu, G. M. Zeng, B. B. Shao, Q. H. Liang, Q. Y. He, X. Z. Yuan, D. L. Huang, M. Chen, *Appl. Catal. B* **2020**, *265*, 118579.
[38] H. W. Kroto, J. R. Heath, S. C. Obrien, R. F. Curl, R. E. Smalley, *Nature* **1985**, *318*, 162 – 163.
[39] M. Park, K. I. Hong, M. Kang, T. W. Kim, H. Lee, W. D. Jang, K. U. Jeong, *ACS Nano* **2019**, *13*, 6101 – 6112.
[40] S. S. Zheng, M. L. Xu, X. Lu, *ACS Appl. Mater. Interfaces* **2015**, *7*, 20285 – 20291.
[41] F. N. Lu, E. A. Neal, T. Nakanishi, *Acc. Chem. Res.* **2019**, *52*, 1834 – 1843.
[42] M. Kohlhaas, M. Zahres, C. Mayer, M. Engeser, C. Merten, J. Niemeyer, *Chem. Commun.* **2019**, *55*, 3298 – 3301.
[43] Y. Q. Feng, X. Wang, J. F. Huang, P. P. Dong, J. Ji, J. Li, L. Y. Cao, L. L. Feng, P. Jin, C. R. Wang, *Chem. Eng. J.* **2020**, *390*, 124525.
[44] G. Saianand, A. I. Gopalan, J. C. Lee, C. Sathish, K. Gopalakrishnan, G. E. Unni, D. Shanbhag, V. Dasireddy, J. B. Yi, S. B. Xi, A. H. Al-Muhtaseb, A. Vinu, *Small* **2020**, *16*, 1903937.
[45] Y. H. Choi, J. Lee, A. Parija, J. S. Cho, S. V. Verkhoturov, M. Al-Hashimi, L. Fang, S. Banerjee, *ACS Catal.* **2016**, *6*, 6246 – 6254.
[46] Z. L. Du, N. Jannatun, D. Y. Yu, J. Ren, W. H. Huang, X. Lu, *Nanoscale* **2018**, *10*, 23070 – 23079.
[47] R. Gao, Q. B. Dai, F. Du, D. P. Yan, L. M. Dai, *J. Am. Chem. Soc.* **2019**, *141*, 11658 – 11666.
[48] J. Liu, H. Q. Wang, M. Antonietti, *Chem. Soc. Rev.* **2016**, *45*, 2308 – 2326.
[49] J. B. Wang, C. Liu, S. Yang, X. Lin, W. L. Shi, *J. Phys. Chem. Solids* **2020**, *136*, 109164.
[50] S. Keshtkar, A. Rashidi, M. Kooti, M. Askarieh, S. Pourhashem, E. Ghasemy, N. Izadi, *Talanta* **2018**, *188*, 531 – 539.
[51] D. Bera, L. Qian, T.-K. Tseng, P. H. Holloway, *Materials* **2010**, *3*, 2260 – 2345.
[52] S. Collavini, J. L. Delgado, *Sustainable Energy Fuels* **2018**, *2*, 2480 – 2493.
[53] S. Ogawa, K. Hu, F.-R. F. Fan, A. J. Bard, *J. Phys. Chem. B* **1997**, *101*, 5707 – 5711.
[54] C. F. Hoener, K. A. Allan, A. J. Bard, A. Campion, M. A. Fox, T. E. Mallouk, S. E. Webber, J. M. White, *J. Phys. Chem.* **1992**, *96*, 3812 – 3817.
[55] A. R. Kortan, R. Hull, R. L. Opila, M. G. Bawendi, M. L. Steigerwald, P. J. Carroll, L. E. Brus, *J. Am. Chem. Soc.* **1990**, *112*, 1327 – 1332.
[56] L. Spanhel, M. A. Anderson, *J. Am. Chem. Soc.* **1991**, *113*, 2826 – 2833.
[57] D. Bera, L. Qian, P. H. Holloway, *J. Phys. D* **2008**, *41*, 182002.
[58] A. Sashchiuk, E. Lifshitz, R. Reisfeld, T. Saraidarov, M. Zelner, A. Willenz, *J. Sol-Gel Sci. Technol.* **2002**, *24*, 31 – 38.
[59] S. Singh, N. Rama, M. S. R. Rao, *Appl. Phys. Lett.* **2006**, *88*, 222111.
[60] Y. Xie, Y. Qian, W. Wang, S. Zhang, Y. Zhang, *Science* **1996**, *272*, 1926 – 1927.
[61] L. Wang, L. Chen, T. Luo, Y. Qian, *Mater. Lett.* **2006**, *60*, 3627 – 3630.
[62] S.-H. Yu, J. Yang, Y.-S. Wu, Z.-H. Han, Y. Xie, Y.-T. Qian, *Mater. Res. Bull.* **1998**, *33*, 1661 – 1666.
[63] D. Battaglia, X. Peng, *Nano Lett.* **2002**, *2*, 1027 – 1030.
[64] D. V. Talapin, A. L. Rogach, A. Kornowski, M. Haase, H. Weller, *Nano Lett.* **2001**, *1*, 207 – 211.
[65] D. V. Talapin, S. Haubold, A. L. Rogach, A. Kornowski, M. Haase, H. Weller, *J. Phys. Chem. B* **2001**, *105*, 2260 – 2263.

[66] W. K. Bae, M. K. Nam, K. Char, S. Lee, *Chem. Mater.* **2008**, *20*, 5307 – 5313.

[67] F. C. Frank, J. H. v. d. Merwe, N. F. Mott, *Proc. R. Soc. London Ser. A* **1949**, *198*, 205 – 216.

[68] M. Volmer, A. Weber, *Z. Phys. Chem.* **1926**, *119U*, 277 – 301.

[69] N. Pradhan, D. Goorskey, J. Thessing, X. Peng, *J. Am. Chem. Soc.* **2005**, *127*, 17586 – 17587.

[70] Z. Yu-Hong, Z. Jian-Hua, B. Jing-Feng, W. Wei-Zhu, J. Yang, W. Xiao-Guang, X. Jian-Bai, *Chin. Phys. Lett.* **2007**, *24*, 2118 – 2121.

[71] S. Hou, X. Zhang, H. Mao, J. Wang, Z. Zhu, W. Jing, *Phys. Status Solidi B* **2009**, *246*, 2333 – 2336.

[72] P. V. Radovanovic, D. R. Gamelin, *J. Am. Chem. Soc.* **2001**, *123*, 12207 – 12214.

[73] L. Wang, J. Han, B. Sundahl, S. Thornton, Y. Zhu, R. Zhou, C. Jaye, H. Liu, Z.-Q. Li, G. T. Taylor, D. A. Fischer, J. Appenzeller, R. J. Harrison, S. S. Wong, *Nanoscale* **2016**, *8*, 15553 – 15570.

[74] K. C. Hwang, D. Mauzerall, *Nature* **1993**, *361*, 138 – 140.

[75] H. Zahra, D. Elmaghroui, I. Fezai, S. Jaziri, *J. Appl. Phys.* **2016**, *120*, 205702.

[76] X. Tang, G. F. Wu, K. W. C. Lai, *Appl. Phys. Lett.* **2017**, *110*, 241104.

[77] R. Narayanan, B. N. Reddy, M. Deepa, *J. Phys. Chem. C* **2012**, *116*, 7189 – 7199.

[78] R. Saran, V. Stolojan, R. J. Curry, *Sci. Rep.* **2014**, *4*, 5041.

[79] Z. Lian, P. Xu, W. Wang, D. Zhang, S. Xiao, X. Li, G. Li, *ACS Appl. Mater. Interfaces* **2015**, *7*, 4533 – 4540.

[80] X. Jiang, M. Yuan, H. Liu, Z. Song, H. Li, Z. Du, *J. Phys. Chem. C* **2017**, *121*, 23676 – 23682.

[81] A. Biswas, I. S. Bayer, A. S. Biris, T. Wang, E. Dervishi, F. Faupel, *Adv. Colloid Interface Sci.* **2012**, *170*, 2 – 27.

[82] M. Sajid, J. Płotka-Wasylka, *Microchem. J.* **2020**, *154*, 104623.

[83] C. Lam, Y. F. Zhang, Y. H. Tang, C. S. Lee, I. Bello, S. T. Lee, *J. Cryst. Growth* **2000**, *220*, 466 – 470.

[84] J. F. de Carvalho, S. N. de Medeiros, M. A. Morales, A. L. Dantas, A. S. Carriço, *Appl. Surf. Sci.* **2013**, *275*, 84 – 87.

[85] T. Asahi, T. Sugiyama, H. Masuhara, *Acc. Chem. Res.* **2008**, *41*, 1790 – 1798.

[86] H. Sheikh Tanzina, C. Ezharul Hoque, *Curr. Drug Delivery* **2018**, *15*, 485 – 496.

[87] F. Mafuné, J.-y. Kohno, Y. Takeda, T. Kondow, H. Sawabe, *J. Phys. Chem. B* **2000**, *104*, 9111 – 9117.

[88] F. Mafuné, J.-y. Kohno, Y. Takeda, T. Kondow, H. Sawabe, *J. Phys. Chem. B* **2001**, *105*, 5114 – 5120.

[89] N. G. Semaltianos, *Crit. Rev. Solid State Sci.* **2010**, *35*, 105 – 124.

[90] H. Wender, L. F. de Oliveira, P. Migowski, A. F. Feil, E. Lissner, M. H. G. Prechtl, S. R. Teixeira, J. Dupont, *J. Phys. Chem. C* **2010**, *114*, 11764 – 11768.

[91] K.-i. Okazaki, T. Kiyama, K. Hirahara, N. Tanaka, S. Kuwabata, T. Torimoto, *Chem. Commun.* **2008**, 691 – 693.

[92] L. Yang, M. P. Seah, E. H. Anstis, I. S. Gilmore, J. L. S. Lee, *J. Phys. Chem. C* **2012**, *116*, 9311 – 9318.

[93] M. Benelmekki, J. Vernieres, J.-H. Kim, R.-E. Diaz, P. Grammatikopoulos, M. Sowwan, *Mater. Chem. Phys.* **2015**, *151*, 275 – 281.

[94] K.-M. Lee, D.-J. Lee, H. Ahn, *Mater. Lett.* **2004**, *58*, 3122 – 3125.

[95] M. Gracia-Pinilla, E. Martínez, G. S. Vidaurri, E. Pérez-Tijerina, *Nanoscale Res. Lett.* **2010**, *5*, 180 – 188.

[96] S. D. Henam, F. Ahmad, M. A. Shah, S. Parveen, A. H. Wani, *Spectrochim. Acta Part A* **2019**, *213*, 337 – 341.

[97] M. Mascolo, Y. Pei, T. Ring, *Materials* **2013**, *6*, 5549 – 5567.

[98] K. Petcharoen, A. Sirivat, *Mater. Sci. Eng. B* **2012**, *177*, 421 – 427.

[99] A. Pradeep, P. Priyadharsini, G. Chandrasekaran, *J. Magn. Magn. Mater.* **2008**, *320*, 2774 – 2779.

[100] Y. Manawi, A. S. Ihsanullah, T. Al-Ansari, M. Atieh, *Materials* **2018**, *11*, 822.

[101] T. J. Daou, G. Pourroy, S. Bégin-Colin, J. M. Grenèche, C. Ulhaq-Bouillet, P. Legaré, P. Bernhardt, C. Leuvrey, G. Rogez, *Chem. Mater.* **2006**, *18*, 4399 – 4404.

[102] H.-C. Chiu, C.-S. Yeh, *J. Phys. Chem. C* **2007**, *111*, 7256 – 7259.

[103] P. K. Sudeep, B. I. Ipe, K. G. Thomas, M. V. George, S. Barazzouk, S. Hotchandani, P. V. Kamat, *Nano Lett.* **2002**, *2*, 29 – 35.

[104] N. L. Dmitruk, O. Y. Borkovskaya, S. V. Mamykin, D. O. Naumenko, N. I. Berezovska, I. M. Dmitruk, V. Meza-Laguna, E. Alvarez-Zauco, E. V. Basiuk, *J. Nanosci. Nanotechnol.* **2008**, *8*, 5958 – 5965.

[105] Y. Yan, J. Gong, J. Chen, Z. Zeng, W. Huang, K. Pu, J. Liu, P. Chen, *Adv. Mater.* **2019**, *31*, 1808283.

[106] K. Chu, Y. P. Liu, Y. B. Li, H. Zhang, Y. Tian, *J. Mater. Chem. A* **2019**, *7*, 4389 – 4394.

[107] Y. P. Liu, Y. B. Li, D. J. Huang, H. Zhang, K. Chu, *Chem. Eur. J.* **2019**, *25*, 11933 – 11939.

[108] Y. Liu, C. L. Liang, J. J. Wu, T. Sharifi, H. Xu, Y. Nakanishi, Y. C. Yang, C. F. Woellne, A. Aliyan, A. A. Marti, B. H. Xie, R. Vajtai, W. Yang, P. M. Ajayan, *Adv. Mater. Interfaces* **2018**, *5*, 1700895.

[109] C. Roth, I. Hussain, M. Bayati, R. J. Nichols, D. J. Schiffrin, *Chem. Commun.* **2004**, 1532 – 1533.

[110] B. Bończak, W. Lisowski, A. Kamińska, M. Hołdyński, M. Fiałkowski, *J. Phys. Chem. C* **2019**, *123*, 6229 – 6240.

[111] J. Shukla, M. R. Ajayakumar, Y. Kumar, P. Mukhopadhyay, *Chem. Commun.* **2018**, *54*, 900 – 903.

[112] Z. C. Lin, H. H. Wang, M. Lei, *Electrocatalysis* **2019**, *10*, 524 – 531.

[113] Z. Y. Bai, M. Shi, L. Niu, Z. C. Li, L. B. Jiang, L. Yang, *J. Nanopart. Res.* **2013**, *15*, 2061.

[114] X. Zhang, L. X. Ma, *J. Power Sources* **2015**, *286*, 400 – 405.

[115] M. R. Benzigar, S. Joseph, A. V. Baskar, D. H. Park, G. Chandra, S. Umapathy, S. N. Talapaneni, A. Vinu, *Adv. Funct. Mater.* **2018**, *28*, 1803701.

[116] M. R. Benzigar, S. Joseph, H. Ilbeygi, D. H. Park, S. Sarkar, G. Chandra, S. Umapathy, S. Srinivasan, S. N. Talapaneni, A. Vinu, *Angew. Chem. Int. Ed.* **2018**, *57*, 569 – 573; *Angew. Chem.* **2018**, *130*, 578 – 582.

[117] Y. Cao, S. Cong, X. Cao, F. Wu, Q. Liu, M. R. Amer, C. Zhou, *Top. Curr. Chem.* **2017**, *375*, 75.

[118] Y. Shen, J. S. Reparaz, M. R. Wagner, A. Hoffmann, C. Thomsen, J.-O. Lee, S. Heeg, B. Hatting, S. Reich, A. Saeki, S. Seki, K. Yoshida, S. S. Babu, H. Möhwald, T. Nakanishi, *Chem. Sci.* **2011**, *2*, 2243 – 2250.

[119] M. Mazloum-Ardakani, A. Khoshroo, *Electrochem. Commun.* **2014**, *42*, 9 – 12.

[120] J. Hao, L. Guan, X. Guo, Y. Lian, S. Zhao, J. Dong, S. Yang, H. Zhang, B. Sun, *J. Nanosci. Nanotechnol.* **2011**, *11*, 7857 – 7862.

[121] M. Naffakh, A. M. Díez-Pascual, M. A. Gómez-Fatou, *J. Mater. Chem.* **2011**, *21*, 7425 – 7433.

[122] D. M. Guldi, E. Menna, M. Maggini, M. Marcaccio, D. Paolucci, F. Paolucci, S. Campidelli, M. Prato, G. M. A. Rahman, S. Schergna, *Chem. Eur. J.* **2006**, *12*, 3975 – 3983.

[123] J. F. Nierengarten, V. Gramlich, F. Cardullo, F. Diederich, *Angew. Chem. Int. Ed. Engl.* **1996**, *35*, 2101 – 2103; *Angew. Chem.* **1996**, *108*, 2242 – 2244.

[124] B. W. Smith, M. Monthioux, D. E. Luzzi, *Nature* **1998**, *396*, 323 – 324.

[125] A. Gloter, K. Suenaga, H. Kataura, R. Fujii, T. Kodama, H. Nishikawa, I. Ikemoto, K. Kikuchi, S. Suzuki, Y. Achiba, S. Iijima, *Chem. Phys. Lett.* **2004**, *390*, 462 – 466.

[126] M. Kalbáč, L. Kavan, M. Zukalová, S. Yang, J. Čech, S. Roth, L. Dunsch, *Chem. Eur. J.* **2007**, *13*, 8811 – 8817.

[127] A. N. Khlobystov, K. Porfyrakis, M. Kanai, D. A. Britz, A. Ardavan, H. Shinohara, T. J. S. Dennis, G. A. D. Briggs, *Angew. Chem. Int. Ed.* **2004**, *43*, 1386 – 1389; *Angew. Chem.* **2004**, *116*, 1410 – 1413.

[128] S. Okada, M. Otani, A. Oshiyama, *Phys. Rev. B* **2003**, *67*, 205411.

[129] T. Shimada, T. Okazaki, R. Taniguchi, T. Sugai, H. Shinohara, K. Suenaga, Y. Ohno, S. Mizuno, S. Kishimoto, T. Mizutani, *Appl. Phys. Lett.* **2002**, *81*, 4067 – 4069.

[130] J. L. Delgado, P. de la Cruz, A. Urbina, J. T. López Navarrete, J. Casado, F. Langa, *Carbon* **2007**, *45*, 2250 – 2252.

[131] K.-S. Liao, J. Wang, D. Früchtl, N. J. Alley, E. Andreoli, E. P. Dillon, A. R. Barron, H. Kim, H. J. Byrne, W. J. Blau, S. A. Curran, *Chem. Phys. Lett.* **2010**, *489*, 207 – 211.

[132] S. Giordani, J.-F. Colomer, F. Cattaruzza, J. Alfonsi, M. Meneghetti, M. Prato, D. Bonifazi, *Carbon* **2009**, *47*, 578 – 588.

[133] A. G. Nasibulin, P. V. Pikhitsa, H. Jiang, D. P. Brown, A. V. Krasheninnikov, A. S. Anisimov, P. Queipo, A. Moisala, D. Gonzalez, G. Lientschnig, A. Hassanien, S. D. Shandakov, G. Lolli, D. E. Resasco, M. Choi, D. Tománek, E. I. Kauppinen, *Nat. Nanotechnol.* **2007**, *2*, 156 – 161.

[134] A. Hasanzadeh, A. Khataee, M. Zarei, Y. F. Zhang, *Sci. Rep.* **2019**, *9*, 13780.

[135] F. D′Souza, R. Chitta, A. S. D. Sandanayaka, N. K. Subbaiyan, L. D′Souza, Y. Araki, O. Ito, *J. Am. Chem. Soc.* **2007**, *129*, 15865 – 15871.

[136] D. M. Guldi, E. Menna, M. Maggini, M. Marcaccio, D. Paolucci, F. Paolucci, S. Campidelli, M. Prato, G. M. A. Rahman, S. Schergna, *Chem. Eur. J.* **2006**, *12*, 3975 – 3983.

[137] M. S. Arnold, J. D. Zimmerman, C. K. Renshaw, X. Xu, R. R. Lunt, C. M. Austin, S. R. Forrest, *Nano Lett.* **2009**, *9*, 3354 – 3358.

[138] M. Rudolf, S. V. Kirner, D. M. Guldi, *Chem. Soc. Rev.* **2016**, *45*, 612 – 630.

[139] A. Cabrera-Espinoza, S. Collavini, J. L. Delgado, *Sustainable Energy Fuels* **2020**, *4*, 3264 – 3281.

[140] A. Rochefort, *Phys. Rev.* **2003**, *67*, 115401.

[141] R. Nakanishi, J. Satoh, K. Katoh, H. T. Zhang, B. K. Breedlove, M. Nishijima, Y. Nakanishi, H. Omachi, H. Shinohara, M. Yamashita, *J. Am. Chem. Soc.* **2018**, *140*, 10955 – 10959.

[142] T. Wei, O. Martin, M. Q. Chen, S. F. Yang, F. Hauke, A. Hirsch, *Angew. Chem. Int. Ed.* **2019**, *58*, 8058 – 8062; *Angew. Chem.* **2019**, *131*, 8142 – 8146.

[143] Y. F. Shen, J. S. Reparaz, M. R. Wagner, A. Hoffmann, C. Thomsen, J. O. Lee, S. Heeg, B. Hatting, S. Reich, A. Saeki, S. Seki, K. Yoshida, S. S. Babu, H. Mohwald, T. Nakanishi, *Chem. Sci.* **2011**, *2*, 2243 – 2250.

[144] V. Strauss, A. Roth, M. Sekita, D. M. Guldi, *Chem* **2016**, *1*, 531 – 556.

[145] A. Hasanzadeh, A. Khataee, M. Zarei, Y. Zhang, *Sci. Rep.* **2019**, *9*, 13780.

[146] R. T. Hu, F. F. Yao, C. X. Wu, C. H. Jin, L. H. Guan, *Sustainable Energy Fuels* **2019**, *3*, 1951 – 1956.

[147] D. D. Liu, L. Tao, D. F. Yan, Y. Q. Zou, S. Y. Wang, *ChemElectroChem* **2018**, *5*, 1775 – 1785.

[148] G. L. Tian, M. Q. Zhao, D. S. Yu, X. Y. Kong, J. Q. Huang, Q. Zhang, F. Wei, *Small* **2014**, *10*, 2251 – 2259.

[149] T. Y. Ma, J. R. Ran, S. Dai, M. Jaroniec, S. Z. Qiao, *Angew. Chem. Int. Ed.* **2015**, *54*, 4646 – 4650; *Angew. Chem.* **2015**, *127*, 4729 – 4733.

[150] S. Y. Wang, D. S. Yu, L. M. Dai, *J. Am. Chem. Soc.* **2011**, *133*, 5182 – 5185.

[151] M. Garrido, J. Calbo, L. Rodríguez-Pérez, J. Aragó, E. Ortí, M. Á. Herranz, N. Martín, *Chem. Commun.* **2017**, *53*, 12402 – 12405.

[152] V. C. Tung, J.-H. Huang, I. Tevis, F. Kim, J. Kim, C.-W. Chu, S. I. Stupp, J. Huang, *J. Am. Chem. Soc.* **2011**, *133*, 4940 – 4947.

[153] B. Thirumalraj, S. Palanisamy, S.-M. Chen, C.-Y. Yang, P. Periakaruppan, B.-S. Lou, *RSC Adv.* **2015**, *5*, 77651 – 77657.

[154] T. Gan, C. Hu, S. Hu, *Anal. Methods* **2014**, *6*, 9220 – 9227.

[155] J. Ma, Q. Guo, H.-L. Gao, X. Qin, *Fullerenes, Nanotubes Carbon Nanostruct.* **2015**, *23*, 477 – 482.

[156] T. Gan, C. Hu, Z. Sun, S. Hu, *Electrochim. Acta* **2013**, *111*, 738 – 745.

[157] L. Song, C. Guo, T. Li, S. Zhang, *Ceram. Int.* **2017**, *43*, 7901 – 7907.

[158] E. Yoo, J. Kim, E. Hosono, H.-s. Zhou, T. Kudo, I. Honma, *Nano Lett.* **2008**, *8*, 2277 – 2282.

[159] G. Jnawali, Y. Rao, J. H. Beck, N. Petrone, I. Kymissis, J. Hone, T. F. Heinz, *ACS Nano* **2015**, *9*, 7175 – 7185.

[160] M. Jung, D. Shin, S.-D. Sohn, S.-Y. Kwon, N. Park, H.-J. Shin, *Nanoscale* **2014**, *6*, 11835 – 11840.

[161] R. Mirzayev, K. Mustonen, M. R. A. Monazam, A. Mittelberger, T. J. Pennycook, C. Mangler, T. Susi, J. Kotakoski, J. C. Meyer, *Sci. Adv.* **2017**, *3*, e1700176.

[162] E. Monazami, L. Bignardi, P. Rudolf, P. Reinke, *Nano Lett.* **2015**, *15*, 7421 – 7430.

[163] K. Ullmann, P. B. Coto, S. Leitherer, A. Molina-Ontoria, N. Martín, M. Thoss, H. B. Weber, *Nano Lett.* **2015**, *15*, 3512 – 3518.

[164] R. Wang, S. G. Wang, X. W. Wang, J. A. S. Meyer, P. Hedegard, B. W. Laursen, Z. H. Cheng, X. H. Qiu, *Small* **2013**, *9*, 2420 – 2426.

[165] P. Song, L. Liu, G. Huang, Y. Yu, Q. Guo, *Nanotechnology* **2013**, *24*, 505706.

[166] J. Yang, M. Heo, H. J. Lee, S.-M. Park, J. Y. Kim, H. S. Shin, *ACS Nano* **2011**, *5*, 8365 – 8371.

[167] C. Ojeda-Aristizabal, E. J. G. Santos, S. Onishi, A. Yan, H. I. Rasool, S. Kahn, Y. Lv, D. W. Latzke, J. Velasco, M. F. Crommie, M. Sorensen, K. Gotlieb, C.-Y. Lin, K. Watanabe, T. Taniguchi, A. Lanzara, A. Zettl, *ACS Nano* **2017**, *11*, 4686 – 4693.

[168] K. Berland, P. Hyldgaard, *Phys. Rev. B* **2013**, *87*, 205421.

[169] K. Kim, T. H. Lee, E. J. G. Santos, P. S. Jo, A. Salleo, Y. Nishi, Z. Bao, *ACS Nano* **2015**, *9*, 5922 – 5928.

[170] M. Neek-Amal, N. Abedpour, S. N. Rasuli, A. Naji, M. R. Ejtehadi, *Phys. Rev. E* **2010**, *82*, 051605.

[171] S. Grimme, C. Mück-Lichtenfeld, J. Antony, *J. Phys. Chem. C* **2007**, *111*, 11199 – 11207.

[172] H. Ma, H. Babaei, Z. Tian, *Carbon* **2019**, *148*, 196 – 203.

[173] X. Zhang, J.-W. Zhang, P.-H. Xiang, J. Qiao, *Appl. Surf. Sci.* **2018**, *440*, 477 – 483.

[174] J. Guan, X. Chen, T. Wei, F. Liu, S. Wang, Q. Yang, Y. Lu, S. Yang, *J. Mater. Chem. A* **2015**, *3*, 4139 – 4146.

[175] X. Zhang, Y. Huang, Y. Wang, Y. Ma, Z. Liu, Y. Chen, *Carbon* **2009**, *47*, 334 – 337.

[176] D. W. Chen, Y. Q. Zou, S. Y. Wang, *Mater. Today Energy* **2019**, *12*, 250 – 268.

[177] N. B. Schorr, J. S. Hui, J. Rodriguez-Lopez, *Curr. Opin. Electrochem.* **2019**, *13*, 100 – 106.

[178] J. Guan, X. Chen, T. Wei, F. P. Liu, S. Wang, Q. Yang, Y. L. Lu, S. F. Yang, *J. Mater. Chem. A* **2015**, *3*, 4139 – 4146.

[179] X. Zhang, X. Z. Yuan, L. B. Jiang, J. Zhang, H. B. Yu, W. Hou, G. M. Zeng, *Chem. Eng. J.* **2020**, *390*, 124475.

[180] P. Ganguly, M. Harb, Z. Cao, L. Cavallo, A. Breen, S. Dervin, D. D. Dionysiou, S. C. Pillai, *ACS Energy Lett.* **2019**, *4*, 1687 – 1709.

[181] J. Kim, H. Lee, J. Y. Lee, K. H. Park, W. Kim, J. H. Lee, H. J. Kang, S. W. Hong, H. J. Park, S. Lee, H. D. Park, J. Y. Kim, Y. W. Jeong, J. Lee, *Appl. Catal. B* **2020**, *270*, 118862.

[182] J. Guan, J. H. Wu, D. C. Jiang, X. J. Zhu, R. N. Guan, X. Y. Lei, P. W. Du, H. L. Zeng, S. F. Yang, *Int. J. Hydrogen Energy* **2018**, *43*, 8698 – 8706.

[183] D. L. Huang, Z. H. Li, G. M. Zeng, C. Y. Zhou, W. J. Xue, X. M. Gong, X. L. Yan, S. Chen, W. J. Wang, M. Cheng, *Appl. Catal. B* **2019**, *240*, 153 – 173.
[184] D. L. Jiang, T. Y. Wang, Q. Xu, D. Li, S. C. Meng, M. Chen, *Appl. Catal. B* **2017**, *201*, 617 – 628.
[185] X. Chen, H. L. Chen, J. Guan, J. M. Zhen, Z. J. Sun, P. W. Du, Y. L. Lu, S. F. Yang, *Nanoscale* **2017**, *9*, 5615 – 5623.

Manuskript erhalten: 8. Juli 2020
Akzeptierte Fassung online: 17. August 2020
Endgültige Fassung online: 8. Oktober 2020